RESEARCH

Check for updates

Probabilistic Modeling and Uncertainty Quantification of Detailed Combustion Simulation for a Swirl Stabilized Spray Burner

Benedict Enderle[1] · Bastian Rauch[1] · Felix Grimm[1] · Georg Eckel[1] · Manfred Aigner[1]

© The Author(s) 2023

Abstract

To enable risk informed decisions in the simulation-based design and development of novel combustors, uncertainties in the simulation results must be considered. However, due to the high computational costs for their quantification, these uncertainties are commonly not taken into account. Therefore, this work aims at applying an efficient methodology for uncertainty quantification based on Polynomial Chaos Expansion to a semi-technical spray burner reflecting characteristics typically found in modern aeroengine combustors. This requires accurate treatment of the multicomponent liquid fuel, a combustion model relying on finite rate chemistry and a scale resolving hybrid turbulence model to account for highly unsteady flow features and combustion. To overcome the need for costly experimental data for the spray boundary conditions, an algebraic primary breakup model is utilized. The resulting reduction in a priori information is compensated through probabilistic modeling and uncertainty quantification. Due to their importance in the design process, temperature distribution in the gas phase as well as the flame position are considered as the primary quantities of interest. For these quantities of interest, moderate uncertainties are found in the probabilistic simulation results. Further, the predictive capability of the simulation model under uncertainties is quantitively assessed by defining accurary metrics for the gas phase temperature prediction. The study further reveals that the imposed input uncertainties affect quantities of interest in both the dispersed and the gas phase through phase coupling effects.

✉ Benedict Enderle
benedict.enderle@dlr.de

[1] German Aerospace Center (DLR), Pfaffenwaldring 38–40, 70569 Stuttgart, Germany

1 Introduction

Anthropogenic emissions from combustion systems are widely recognized as a leading contributor to global climate change. To mitigate the environmental impact of aviation and comply with increasingly strict regulatory policies, improving the performance of combustion systems in aeroengines has become a key challenge. In this regard, virtual simulation tools play an important role for the efficient exploration of the design space when considering novel combustor concepts in the design process. As such design processes are inherently exploratory, many input parameters to the simulation tools are uncertain or even unknown beforehand due to lack of knowledge regarding the final design. This induces uncertainties in the simulation results which should be quantified and taken into consideration. Only on the basis of this additional information, risk-informed decisions can be made to ensure optimal and safe operation.

A key aspect regarding aeroengine safety and emissions is fuel injection and distribution in the combustor (Dryer 2015; Hubbard and Denny 1975; Lefebvre 2010), i.e. the reliable atomization of the liquid fuel into a spray of droplets. Subsequent processes from evaporation up to pollutant formation strongly depend on the quality of the spray (Lefebvre 1988). In simulations, this must be reflected in accurate boundary conditions regarding droplet size, velocity and local volume flux. However, this data is difficult to acquire from experiments (Tropea 2011) and often relies on expert opinion and experience in early stages of the design process. The influence of incomplete knowledge regarding the spray boundary condition on simulation results was mentioned for example by Eckel and Grohmann (2019), Ruoff et al. (2019), or Pei and Davis (2015), but no systematic assessment in terms of uncertainties in the simulation results was reported.

For this purpose, uncertainty quantification (UQ) aims at quantitatively characterizing the uncertainties in simulation results. In recent times, probabilistic methods have become increasingly popular for the treatment and quantification of uncertainties (Loeven et al. 2007; Red-Horse and Benjamin 2004). In this approach, uncertain input quantities are treated as random variables which can be characterized by probability density functions or intervals to portray their probabilistic behavior. Uncertainties in the output, i.e. the simulation results, are then derived as random variables. As a result, minimum/maximum or confidence intervals can be reported in addition to the simulation results to support the decision makers.

While Monte Carlo simulations are a straightforward method for analyzing the complex mapping between input and output uncertainties, the computational cost of each simulation run in the case of reacting multiphase flows is prohibitively high. Therefore, surrogate models must be used in lieu of the high fidelity simulation model for the propagation of the input uncertainties. An adequate representation of the forward model observables as well as computational efficiency are the main characteristics of such surrogate models. Among the various models proposed in the literature (Forrester and Keane 2008; Yondo and Andrés 2018), Polynomial Chaos Expansion (PCE) in combination with sparse quadrature approaches (Le Maître and Knio 2010) have drawn increasing attention for the use in UQ (Najm 2009; Sheen and Wang 2011; de Souza and Colaço 2014). While the prediction accuracy of data-driven approaches such as Gaussian process regresssion depends on the underlying sampling strategy of the high fidelity simulation model, the PCE and sparse quadrature combination already dictates the most efficient sampling strategy through the quadrature points for PCE construction. Although the PCE methodology is applicable for both intrusive and non-intrusive UQ, the

work at hand is focused on the latter approach, in which an existing simulation code is treated as a black box rather than reformulating the governing equations in a stochastic framework.

Early results of UQ studies for reacting flow simulations were reported for example by Reagan and Najm (2003) and Duraisamy and Alonso (2012), but were limited to gas phase combustion. Pei and Davis (2015) investigated the sensitivity of spray distribution in the Engine Combustion Network (ECN) experimental configuration on parameters of the spray boundary condition under non-reacting conditions. In a similar study, Van Dam and Rutland (2016) analyzed the uncertainties in the LES results for liquid and vapor penetration from a multi-hole gasoline injector. They considered selected parameters for the primary breakup model as input uncertainties to the LES. Further UQ results from the field of combustion simulation covering sub-phenomena such as thermoacoustic (Guo et al. 2018), chemical kinetics (Mueller and Iaccarino 2013) and droplet evaporation (Ruoff et al. 2020) are available in the literature. The use of PCE in detailed combustion simulations for a laboratory-scale turbulent methane/hydrogen bluff-body flame was demonstrated by Khalil and Lacaze (2015), focusing on uncertainties in LES modeling parameters. Furthermore, Masquelet et al. (2017) reported PCE-based UQ results for an industrial scale aviation gas turbine combustor. However, due to the assumption of fast evaporation of the fuel, the multiphase spray regime was not explicitly simulated. A comprehensive UQ study of spray combustion simulations including detailed modeling of the multiphase regime with a distinct focus on the specification of spray boundary conditions is available from (Enderle and Rauch 2020). In this work, a well characterized laboratory-scale spray flame for liquid ethanol was studied. Uncertainties and sensitivities in temperature profiles over the reaction zone were analyzed using PCE. It was shown that these uncertainties mainly arise from the imprecise knowledge concerning the spray cone angle in the spray boundary condition.

The objective of this study is to extend the PCE-based UQ methodology to a complex, semi-technical use case of spray combustion, which is critical for developing innovative aero-engine combustors. The approach employs uncertainty quantification and probabilistic modeling to improve the accuracy of a simulation model when only limited information is available on the spray boundary condition. Hence, this work addresses the aforementioned challenges in the design process, where some inputs to the simulation model are uncertain due to the lack of knowledge regarding the final design, thereby demonstrating the practical applicability of the proposed methodology. Resolving unsteady and non-linear features in flow fields is crucial for (semi)-technical use cases, which necessitates a scale-resolving simulation approach. To this end, the present study aims to demonstrate the feasibility of the proposed UQ methodology in dealing with simulation problems that have high computational costs, thus highlighting its practical utility in such cases.

The remainder of this paper is organized as follows. A brief summary of the methodology for the simulation of turbulent spray combustion is given in Sect. 2, followed by the methods used for PCE-based uncertainty quantification in Sect. 3. These methods are then applied to the DLR Standard Spray Burner (Grohmann and Rauch 2017) in Sect. 4 in which the simulation setup is briefly validated against experimental data for the non-reacting case, followed by detailed UQ results for the reacting multiphase flow. Finally, concluding remarks are drawn in Sect. 5.

2 Methodology for the Simulation of Turbulent Spray Combustion

For the simulation of turbulent spray combustion a computational platform consisting of separate simulation codes for the gaseous and dispersed phase is utilized. Data is exchanged online via two-way coupling of both phases.

2.1 Gas Flow Solver

The Favre filtered transport equations for mass, momentum, enthalpy and species mass fractions in the gas phase are solved by means of the DLR in-house code THETA (Turbulent Heat Release Extension of the TAU Code) (Di Domenico et al. 2011; Domenico 2008). THETA is an incompressible 3D finite volume solver for structured and unstructured dual grids. A second order accurate solution method is achieved by combining the Crank-Nicolson time discretization scheme with central differencing for the convective and diffusive fluxes. The pressure–velocity coupling is based on a projection method.

To account for the complex three-dimensional and unsteady flow features typically found in swirling flames, a hybrid URANS/LES method based on the Scale Adaptive Simulation (SAS) approach as introduced by Menter et al. (2003a) is utilized. The general SAS concept relies on dynamic transitioning between URANS and LES based on the ratio of turbulent lenth scale $\mathscr{L}_t$ to the von Karman length scale $\mathscr{L}_{vK}$. The transition is achieved by introducing a source term to the transport equation of the dissipative turbulence scale in the underlying URANS turbulence model. The SAS model for the work at hand relies on the $k - \omega$-SST turbulence model (Menter and Egorov 2005; Menter et al. 2003b). The additional source term $F_{SST-SAS}$ for the ω transport equation reads

$$F_{SST-SAS} = \max\left[C_{F_1} k S^2 \frac{\mathscr{L}_t}{\mathscr{L}_{vK}} - \frac{2}{C_{F_2}} k \max\left(\frac{1}{\omega^2} \frac{\partial \omega}{\partial x_j} \frac{\partial \omega}{\partial x_j}, \frac{1}{k^2} \frac{\partial k}{\partial x_j} \frac{\partial k}{\partial x_j} \right), 0 \right]. \tag{1}$$

$C_{F,i}$ are modeling constants, $\mathscr{L}_t = \sqrt{k}/\omega$ is the turbulent length scale, S denotes the norm of the strain tensor and $\mathscr{L}_{vK}$ is the von Karman length scale with

$$\mathscr{L}_{vK} = \max\left(\kappa \frac{\sqrt{2S_{ij}S_{ij}}}{\sqrt{\frac{\partial^2 u_i}{\partial x_k^2} \frac{\partial^2 u_i}{\partial x_j^2}}}, C_s \sqrt{\frac{\kappa \hat{\zeta}}{\beta_{\omega_2/\beta_k} - \gamma_2}} \Delta \right). \tag{2}$$

This formulation allows $\mathscr{L}_{vK}$ to adjust to the already resolved scales in a simulation (Menter and Egorov 2005) and provides a length-scale which is proportional to the size of the resolved eddies with consideration of the local grid spacing Δ. In high turbulence regions, the source term $F_{SST-SAS}$ therefore increases and the modeled turbulent viscosity is damped by ω. Ultimately, the dissipating effect of the turbulent viscosity on the resolved fluctuations is reduced.

2.1.1 Combustion Modeling

Chemical reactions of the gas phase species are modeled by a finite-rate combustion (FRC) approach in which a separate transport equation is solved for each species α (Gerlinger 2005). Reaction rate coefficients are calculated during the simulation instead of a priori tabulation. The chemical source term from the FRC model is given by

$$\omega_\alpha(T, Y) = M_\alpha \sum_{r=1}^{N_r} \left(v''_{\alpha,r} - v'_{\alpha,r} \right) \left[\langle k_{f,r} \rangle \prod_{\beta=1}^{N_{sp}} C_\beta^{v'_{\beta,r}} - \langle k_{b,r} \rangle \prod_{\beta=1}^{N_{sp}} C_\beta^{v''_{\beta,r}} \right]. \tag{3}$$

M_α is the molar mass of species α, N_r the number of reactions and v are the stochiometric coefficients. Terms in square brackets denote sources of reactions which are controlled by the forward and backward rate coefficients k_f and k_b. They are calculated using the Arrhenius law (Poinsot and Veynante 2005).

For the application of the FRC model in the context of hybrid URANS/LES, a filtered formulation of the source term from Eq. (3) and a closure for the subgrid contribution is required. For this purpose, subgrid-scale turbulence-chemistry interaction is included using an assumed PDF model (APDF) following Girimaji (1991). This requires the solution of two additional transport equations for the temperature variance and the sum of species variances, as detailed in the work of Gerlinger (2005). The filtered chemical source term then reads

$$\overline{\omega}_\alpha^{FRC-APDF} = \int_{-\infty}^{\infty} \int_{-\infty}^{\infty} \omega_\alpha(\hat{T}, \hat{Y}) P(\hat{T}) P(\hat{Y}) \, \mathrm{d}\hat{T} \mathrm{d}\hat{Y}, \tag{4}$$

where P is an assumed PDF and $\hat{\bullet}$ denotes a random variable. It is assumed that the temperature fluctuation follows a clipped Gaussian PDF while the species' mass fraction fluctuations follow a multivariate β-PDF (Domenico 2008). For further analysis of the APDF model in the context of Scale Adaptive Simulations, the reader is referred to the work of Lourier et al. (2015).

2.1.2 Chemical Reaction Mechanism

After vaporization, species from the CTM fuel families are mapped to equivalent species in the gas phase. Normal-alkanes, cyclo-alkanes and mono-aromatics are assigned to normal-decane, iso-octane and toluene, respectively. These species form the main fuel species in a detailed reaction mechanism comprising 49 species and 300 reactions. The mechanism is based on the work of Slavinskaya (2008) and has been optimized for enhanced stability and computational speed using a linear transformation method (Methling 2017). Furthermore, a sub-mechanism for the formation of the OH^* radical by Kathrotia (2011) is included.

2.2 Dispersed Phase Solver

The dispersed phase, i.e. the evaporating fuel droplets, is computed using the DLR in-house simulation code SPRAYSIM which is based on particle tracking in a Lagrangian reference frame. Subsets of physical fuel droplets with equal properties are approximated by numerical particles and treated as point sources. In this simplification, particles are assumed to be

discrete points providing point sources and point forces to the gas field (Jenny and Roe-kaerts 2012). The coupled ordinary differential equations for the particles' position $\vec{x}_p$, velocity $\vec{u}_p$, diameter d_p, and temperature T_p along their trajectories are solved by a predictor-corrector scheme.

Secondary breakup of the particles is modeled by the Cascade Atomization and Breakup (CAB) model (Tanner 2003). Unresolved subgrid scale velocity fluctuations of the particles are accounted for using the droplet dispersion model proposed by Bini and Jones (2008).

2.2.1 Multicomponent Vaporization Model

In order to capture the complex composition of aviation fuels (Dryer 2015), a multicomponent vaporization model based on Continuous Thermodynamics (CTM) (Doué et al. 2006) is selected. It approximates the properties of the wide range of liquid species typically found in Jet A-1 via distribution functions and representative fuel families. A Γ-PDF is chosen as distribution function and three species families are considered, namely normal-alkanes, cyclo-alkanes and mono-aromatics. The three PDFs were calibrated to match the corresponding two-dimensional gas chromatography (GCxGC) data for Jet A-1. A comparison between experimental data (bars) and CTM approximation (lines) is shown in Fig. 1 for the distribution of mole fraction over the normal boiling point. By this approach, the number of degrees of freedom which need to be calculated in the vaporization model reduces by orders of magnitude. The underlying vaporization model resembles the model by Abramzon and Sirignano (1989) in which rapid mixing within the droplet is assumed. Transformed equations of the vaporization model for the use with CTM are detailed in the work of Eckel and Grohmann (2019).

The mass change due to evaporation leads to mass source terms in the gas field equations which are exchanged between the solvers at each time step.

2.2.2 Modeling of Prefilming Airblast Atomization

The PAMELA (Primary Atomization Model for prEfilming airbLAst injector) model as introduced by Chaussonnet and Vermorel (2016) and Chaussonnet (2014) provides a droplet size distribution characteristic for the spray from prefilming airblast atomizers. An overview of such an atomizer is given in Fig. 2a.

In this phenomenological model, a Rosin-Rammler (RR) function

Fig. 1 Continuous description of Jet A-1 composition using three Γ-PDFs. GCxGC data (bars), CTM fuel families (lines)

(a) Prefilming airblast atomizer   (b) Detail at the atomizing edge
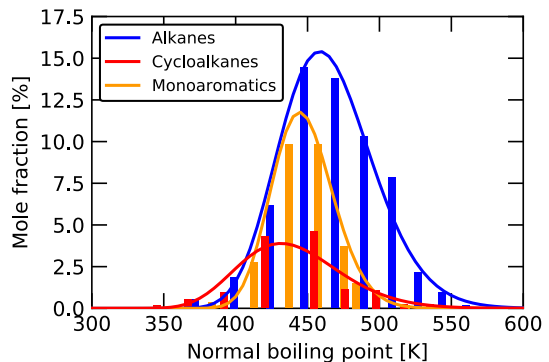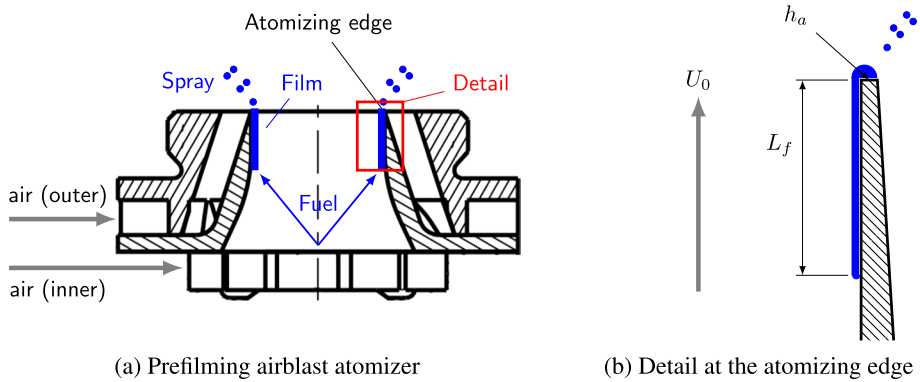
Fig. 2 Typical airblast atomizer as considered in the PAMELA model

$$F_{3,RR}(D) = 1 - \exp\left[-\left(\frac{D}{m}\right)^q\right],$$ (5)

is assumed for the distribution of the droplet diameter. More specifically, Eq. (5) denotes the cumulative volume distribution function for a Rosin-Rammler distribution with the two parameters m and q being the mean value and its spread. These parameters are calculated from geometrical features of the atomizer, namely the thickness h_a of the atomizing edge, the film length L_f and the mean air velocity U_G alongside the film. Figure 2b illustrates these parameters as a detail of the pre-filming airblast atomizer. For the work at hand, the *global* formulation of the PAMELA model is utilized, i.e. calculations based on steady-state mean values.

Constitutive equations for the PAMELA model were derived from the analysis of an academic experiment of liquid film breakup at an atomizing edge (Müller and Meier 2004) consisting of a planar wing-shaped pre-filmer over which a liquid film was atomized. Simultaneous measurements of the film length, air velocity and resulting spray established a database for a wide range of operating conditions (Gepperth et al. 2010).

In this database, a correlation between D_{32}/h_a and We_{h_a} is observed:

$$\frac{D_{32}}{h_a} = \frac{C_1}{\sqrt{\text{We}_{h_a}}}.$$ (6)

We_{h_a} denotes the Weber number with respect to the atomizing edge h_a

$$\text{We}_{h_a} = \frac{\rho_g h_a (r_\rho U_G)^2}{\sigma}$$ (7)

and r_ρ is the ratio of liquid and gas densities:

$$r_\rho = \frac{\sqrt{\rho_l}}{\sqrt{\rho_l} + \sqrt{\rho_g}}.$$ (8)

As aforementioned, it is assumed that the spray after the atomizing edge follows a Rosin-Rammler distribution with parameters q_{PAM} and m_{PAM}. In this case, a relation between D_{32} and the distribution parameters is given by

$$D_{32}^{RR} = m \frac{\Gamma(3/q + 1)}{\Gamma(2/q + 1)} \tag{9}$$

see Lefebvre (2010). Combining Eqs. (9) and (6) yields:

$$m_{\text{PAM}} = C_1 \frac{h_a}{\sqrt{\text{We}_{h_a}}} \frac{\Gamma(2/q + 1)}{\Gamma(3/q + 1)}, \tag{10}$$

in which C_1 is a calibration constant. As mentioned before, q describes the dispersion of the drop size in the spray. Therefore, this parameter cannot be formally linked to a single measurement value (Chaussonnet 2014). A correlation function for q is obtained from fitting of the Rosin-Rammler distribution to the sprays from the database and comparison with the aerodynamic Weber number We_δ based on the boundary layer thickness δ at the atomizing edge,

$$\text{We}_\delta = \frac{\rho_g \delta U_G^2}{\sigma}. \tag{11}$$

The thickness δ is defined according to the work of Gepperth et al. (2010) as

$$\delta = 0.16 \frac{L_f}{\text{Re}_{L_f}^{\frac{1}{7}}} \qquad \text{with} \qquad \text{Re}_{L_f} = \frac{U_G L_f}{\nu_g}. \tag{12}$$

The correlation for q_{PAM} finally reads

$$q_{\text{PAM}} = \frac{C_2}{\sqrt{\text{We}_\delta}} + \left(\frac{h_a}{C_3}\right)^2 + C_4. \tag{13}$$

Again, C_2, C_3 and C_4 are calibration constants. Constants for the PAMELA model from fitting against the experimental database are summarized in Table 1.

3 Methodology for Uncertainty Quantification

Uncertainty quantification aims at identifying the variance in the vector of quantities of interest $\boldsymbol{q} = \{q_1, q_2, q_3, ..\}$ calculated from a simulation model $\mathcal{M}$ with

$$\boldsymbol{x} :\mapsto \boldsymbol{q} = \mathcal{M}(\boldsymbol{x}). \tag{14}$$

Equation (14) describes the deterministic mapping of the inputs $\boldsymbol{x} = \{x_1, x_2, x_3, ..., x_{n_x}\}$ to the quantities of interest. In practical applications, $\mathcal{M}$ may have arbitrary complexity, including several sub-models $\mathcal{M}_{s,i}$ with $\mathcal{M}_{s,i} \subset \mathcal{M}$.

Possible sources of uncertainties in the mapping from Eq. (14) are generally subdivided into model form uncertainties, numerical uncertainties and input

Table 1 Fitting constants in the PAMELA model	C_1 [–]	C_2 [–]	C_3 [mm]	C_4 [–]
	2.01	9.74	5.99	1.77×10^{-2}

uncertainties (Roy and Oberkampf 2011). While model form uncertainties stem from the approximation of the physical system by $\mathscr{M}$, numerical uncertainties are introduced by the numerical solution methods for the underlying set of non-linear differential equations. Finally, input uncertainties describe variations in the vector $\boldsymbol{x}$ comprising initial and boundary conditions as well as model parameters. The present work exclusively focuses on the latter type of uncertainties, since input uncertainties are the dominant type in the design process of aeroengine combustors.

For this purpose, a probabilistic approach is adopted in which uncertainties in $\boldsymbol{x}$ and $\boldsymbol{q}$ are characterized by random variables X and Q over a sample space Ω. Statistical measures regarding the simulation results can then be derived from Q. Hence, the probabilistic formulation of Eq. (14) reads

$$X :\mapsto Q = \mathscr{M}(X). \tag{15}$$

A straight-forward technique to explore this mapping is the well established Monte Carlo method (Fishman 2013), in which Eq. (15) is reconstructed from a series of deterministic model evaluations

$$\boldsymbol{x}^{(i)} :\mapsto \boldsymbol{q}^{(i)} = \mathscr{M}(\boldsymbol{x}^{(i)}). \tag{16}$$

In this approach, the evaluation points $\boldsymbol{x}^{(i)}$ are drawn at random from Ω or placed following sampling strategies such as Latin Hypercube Sampling (McKay and Beckman 1979) or low discrepancy series (Sobol and Asotsky 2011). Major drawbacks of these sampling-based methods are the relatively low convergence rate of higher moments in Q (Le Maître and Knio 2017) and the *curse of dimensionality* (Bengtsson et al. 2008) when facing high dimensional random variables for X. This requires a large set of model evaluations which may be infeasible for computationally expensive models. As an alternative to the direct sampling approach, stochastic spectral methods based on non-intrusive polynomial chaos expansion (PCE) are utilized in the work at hand for the evaluation of Eq. (15).

3.1 Polynomial Chaos Expansion

In contrast to the direct sampling approach, PCE aims at directly reconstructing the functional dependence of the output quantity Q on the stochastic input X (Sudret 2007) making it popular for the use in uncertainty quantification and probabilistic modeling (Najm 2009; Reagan and Najm 2004).

PCE utilizes the fact that the random variable Q can be expressed as a spectral expansion in terms of orthogonal functions of a vector of standard random variables $\boldsymbol{\xi} = \{\xi_1, \xi_2, .., \xi_n\}$ conditional on X (Ghanem and Spanos 1991). The polynomial chaos expansion of Q then reads

$$Q(\boldsymbol{\xi}) = \sum_{k=0}^{\infty} \alpha_k \boldsymbol{\Psi}_k(\xi_1, \xi_2, ...), \tag{17}$$

where α_k are deterministic expansion coefficients and $\boldsymbol{\Psi}_k$ are multivariate polynomials of $\boldsymbol{\xi}$, forming a complete orthogonal basis with respect to the measure on $\boldsymbol{\xi}$ (Khalil and Lacaze 2015). For practical computations, the infinite series from Eq. (17) is typically truncated to a certain order, hence

$$Q = \mathcal{M}(\boldsymbol{\xi}) \approx \sum_{k=0}^{P} \alpha_k \boldsymbol{\Psi}_k\big(\xi_1, \xi_2, ..., \xi_n\big) = \sum_{k=0}^{P} \alpha_k \boldsymbol{\Psi}_k(\boldsymbol{\xi}). \tag{18}$$

Applying a projection method (Ghanem and Ghiocel 1998) and taking advantage of the orthogonality constraint on $\boldsymbol{\Psi}_k$, the expansion coefficients are given as

$$\alpha_k = \frac{1}{\langle \boldsymbol{\Psi}_k, \boldsymbol{\Psi}_k \rangle} \int_{\boldsymbol{\Omega}} \mathcal{M}(\boldsymbol{\xi}) \boldsymbol{\Psi}_k(\boldsymbol{\xi}) \mathcal{P}(\boldsymbol{\xi}) \, \mathrm{d}\boldsymbol{\xi}. \tag{19}$$

Since the inner product $\langle \boldsymbol{\Psi}_k, \boldsymbol{\Psi}_k \rangle$ is known analytically from the choice of Ψ_k, the primary computational effort resides in evaluating the multidimensional integral over Ω. The order of accuracy of the numerical integration directly provides a measure for the accuracy of the PCE. For the work at hand, multidimensional numerical integration based on the Smolyak sparse grid tensorization method (Le Maître and Knio 2010) in combination with a nested Gauss-Patterson quadrature rule (Davis and Rabinowitz 2007) is used. This involves evaluating Eq. (14) at each integration point, i.e. running the actual CFD simulation.

While expectation $\mathbb{E}$ and standard deviation $\mathbb{V}$ of Q can be directly computed from the expansion coefficients by

$$\mathbb{E}[Q] \approx \alpha_0 \quad \text{and} \quad \mathbb{V}[Q] \approx \sum_{k=1}^{P} \alpha_k^2 \langle \Psi_k^2 \rangle, \tag{20}$$

the full posterior distribution $\mathcal{P}(Q)$ is inferred from space filling sampling of the PCE following the density assumed for ξ_i.

3.2 Accuracy Metrics for Uncertain Predictions

The quantitative comparison of observations and uncertain predictions, i.e. experimental data and uncertain simulation results, demands for validation metrics which take into account the probabilistic structure of the uncertain predictions. Two validation metrics are utilized to evaluate the quality of uncertain predictions:

3.2.1 Deterministic Observations

In the case of deterministic observations, for example experimental data without measurement uncertainties, the *Continous Rankend Probabibilty Score* (CRPS) (Gneiting and Raftery 2007) evaluates the difference between the CDF of the uncertain prediction and the idealized perfect observation. The CRPS is defined as

$$\mathrm{CRPS} = \int_{-\infty}^{\infty} \big(\mathcal{C}_Q(\chi) - \mathbb{H}(\chi - q_{obs}) \big)^2 \mathrm{d}\chi, \tag{21}$$

where $\mathcal{C}_Q$ is the CDF of the uncertain prediction of a QoI q, q_{obs} is the certain observation of q and $\mathbb{H}$ denotes the Heaviside function. Therefore, the CRPS yields a generalized mean absolute error in case of uncertain predictions.

3.2.2 Uncertain Observations

In contrast, the *Wasserstein-1* metric W_1 is utilized to compare the probability structure of an uncertain prediction Q with an uncertain observation Q_{obs}. A typical example for an uncertain observation could be experimental data with measurement errors. In the Euclidian space, the quantity $W_1(Q, Q_{obs})$ can be interpreted as the minimum amount of work that is required to turn the respective distribution $\mathscr{C}_Q$ into $\mathscr{C}_{Q_{obs}}$ (Johnson and Wu 2017). In case of one-dimensional distributions on the real line, W_1 can be written in explicit form as

$$W_1 = \int_0^1 |\mathscr{C}_Q^{-1}(\Xi) - \mathscr{C}_{Q_{obs}}^{-1}(\Xi)| \mathrm{d}\Xi. \tag{22}$$

In this equation $\mathscr{C}_Q^{-1}$ and $\mathscr{C}_{Q_{obs}}^{-1}$ are the corresponding inversions of $\mathscr{C}_Q$ and $\mathscr{C}_{Q_{obs}}$. For further derivations, the reader is referred to the work of Bobkov and Ledoux (2014).

3.3 Sensitivity Analysis: Sobol' Indices

Variance-based sensitivity methods such as Sobol' indices (Sobol 1993) offer insight into the sensitivity structure of a given quantity of interest Q. Through this approach, the sensitivity of the simulation results to the different uncertainties in the input can be assessed. Sobol' indices are based on the decomposition of the total variance $\mathbb{V}$ of a model output $\mathscr{M}(\xi)$ into contributions from the different inputs $\mathbb{V}[\mathscr{M}(\xi)|\xi_i]$. We consider the first order indices S_i which account for the direct contribution to the variance of $\mathscr{M}$ from ξ_i, and the total-effect index S_i^T (Homma and Saltelli 1996) which also includes interaction effects of ξ_i with $\xi_{\neq i}$:

$$S_{1,i} = \frac{\mathbb{V}\big[\mathbb{E}\big[\mathscr{M}(\xi)|\xi_i\big]\big]}{\mathbb{V}[\mathscr{M}(\xi)]}, \quad S_i^T = \frac{\mathbb{V}\big[\mathscr{M}(\xi)|\xi_{\sim i}\big]}{\mathbb{V}[\mathscr{M}(\xi)]}. \tag{23}$$

Note that $S_{1,i} \leq S_i^T$. In the case of a Polynomial Chaos Expansion for Q, first order and total Sobol' indices can be computed directly from the expansion coefficients α_k exploiting Eq. (20).

4 Application

4.1 Test Case

The DLR *Standard Spray Burner* (SSB) (Grohmann and Rauch 2017) reflects characteristics typically found in aero-engine combustors, while keeping the geometrical complexity on a semi-technical level. These characteristics include, among others, a complex multi-component fuel, pre-filming airblast atomization, flame confinement through combustor walls and a swirl-dominated flow field for the purpose of flame stabilization. Grohmann and Rauch (2017) and Cantu and Grohmann (2018) reported detailed experimental results for a variety of single component fuels as well as conventional Jet A-1.

Figure 3 provides an overview of the experimental apparatus and a detail of the airblast atomizer. The combustor consists of two distinct components: an air nozzle equipped with
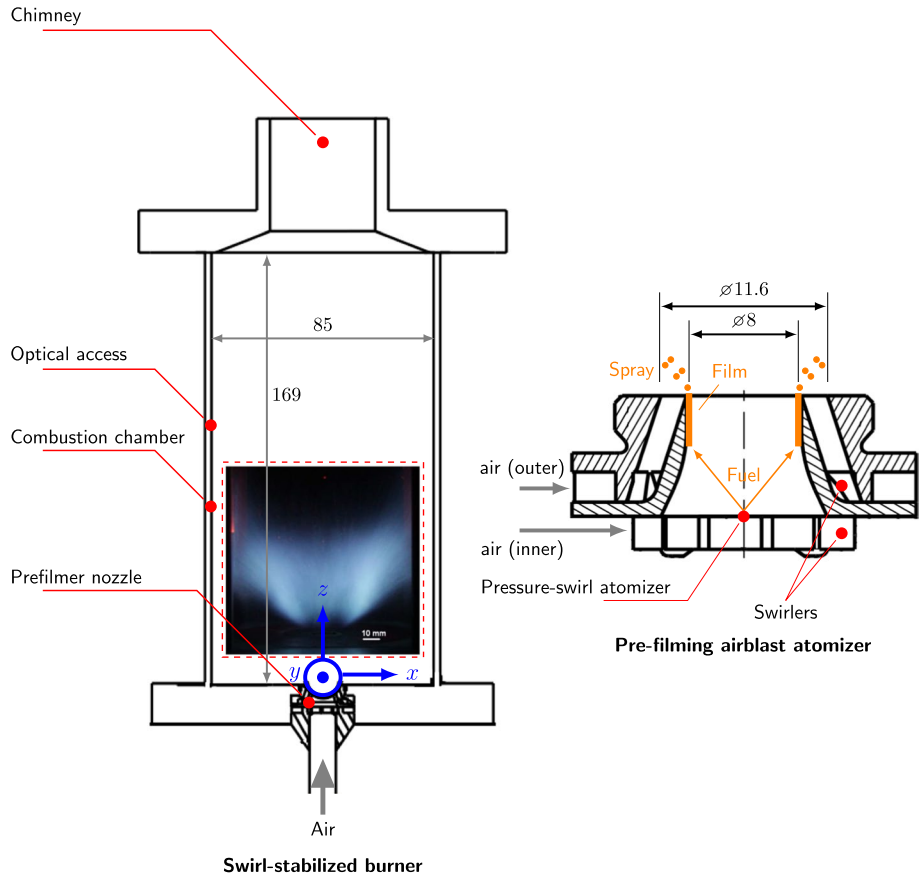
Fig. 3 Sketch and detail of the swirl-stabilized *Standard Spray Burner*

a pre-filming airblast atomizer and a rectangular combustion chamber with a cross section of 85 mm × 85 mm and a height of 169 mm facilitating optical access to the reaction zone through four quartz glass windows. At the top, the cross section of the combustion chamber reduces to a duct (chimney) with 40 mm in diameter to ensure well defined outflow conditions. In the air nozzle, an inner and outer swirler consisting of quadratic swirl vanes provide air for atomization and the formation of a co-rotating swirling flow inside the combustion chamber. Geometrical swirl numbers of $Sw_i = 1.17$ and $Sw_o = 1.22$ were reported for the inner and outer swirler, respectively (Grohmann et al. 2016). In the center of the air nozzle, a primary pressure-swirl injector (Schlick Mod. 121) ejects fuel droplets onto the pre-filmer surface on which a liquid film evolves and finally disintegrates into a fine spray at the atomizing edge. At the exit plane, the inner and outer air nozzles have a diameter of $D_i = 8$ mm and $D_o = 11.6$ mm, respectively.

The comprehensive experimental database for the SSB includes a characterization of the flow field from PIV, temperature profiles over the reaction zone obtained by CARS and dispersed phase data from PDA. Furthermore, a qualitative portrayal of the reaction zone is available from the line-of-sight integrated signal of CH^* chemiluminescence. Due to the challenges for PIV in the presence of additional fine fuel droplets, PIV was only conducted

Table 2 Operating conditions of the baseline Jet A-1 case

Fuel		Jet A-1	
Fuel temperature	T_f	303	[K]
Fuel mass flow rate	$\dot{m}_f$	850	[g/h]
Oxidizer	Air		
Air pressure	p_{air}	1.0	[bar]
Air temperature	T_{air}	323	[K]
Air volume flow rate	$\dot{V}_{air}$	200	[l/min]
Global equivalence ratio	ϕ	0.8	[−]
Thermal input	P_{th}	10.2	[kW]

for the non-reacting flow field. For the work at hand, the *baseline* case for Jet A-1 as summarized in Table 2 is considered.

4.2 Computational Domain and Numerical Setup

The computational domain for the simulation comprises the air nozzle, the quadratic combustion chamber and the outlet chimney. In addition, the air plenum from which the preheated air is fed to the swirler stages is included to obtain a well defined inflow region at the plenum inlet.

An unstructured grid consisting of approximately 1.2 million nodes, corresponding to 5.7 million cells, provides the spatial discretization of the aforementioned computational domain. The grid mainly consists of tetrahedral cells augmented with 4 prismatic layers alongside the walls and hexahedron cells in regions with a distinct flow region (inlet plenum, swirler vanes, outlet duct). Cell sizes range between 0.4 mm in the swirler region and 3.0 mm towards the outlet. The flame zone contains a mesh refinement in the magnitude of 0.75 mm. Figure 4 provides an overview of the grid in a central plane including a detail at the atomizing edge of the air nozzle.

Inlet boundary conditions for the gas phase are given in Table 2. Wall temperatures of the combustion chamber were experimentally determined by phosphor thermometry (Nau et al. 2019). Following the results of Eckel and Grohmann (2019), the bottom plate of the combustion chamber is divided into three zones. According to the measured temperatures in these zones, the temperatures are set to a constant value of $T = 717$ K, $T = 901$ K and $T = 831$ K in the central part, the glowing ring and the corners of the bottom plate,
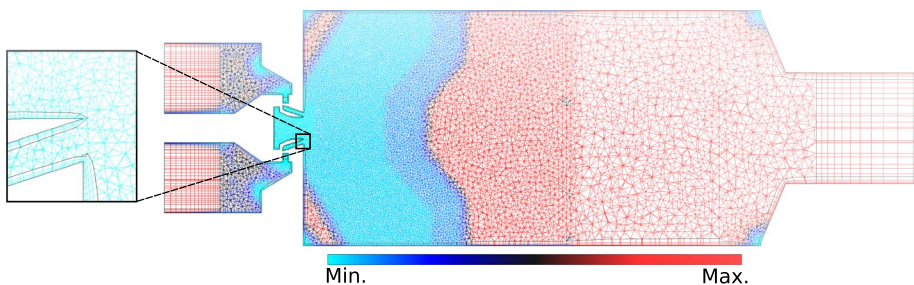
Fig. 4 Distribution of cell sizes in a central plane

(a) Combustion chamber walls   (b) Combustion chamber baseplate
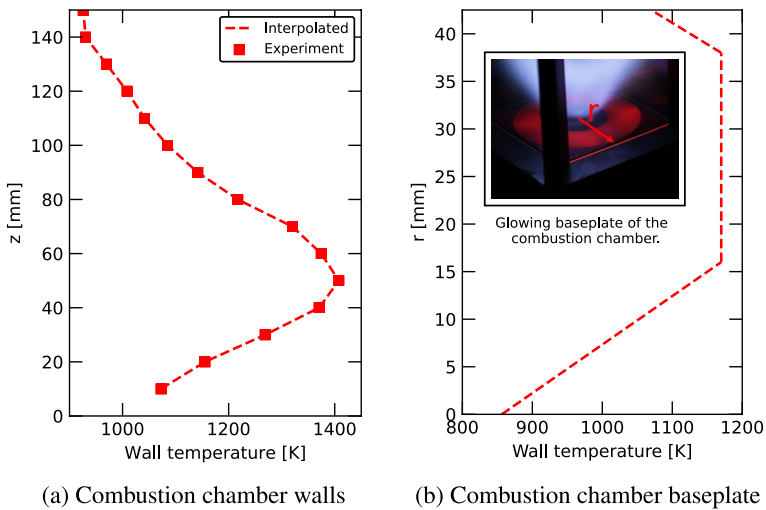
Fig. 5 Temperature profiles for the isothermal boundary condition in the combustion chamber

respectively. Based on the thermometry data, a temperature profile in dependence of the axial direction is imposed at the combustor sidewalls. Resulting temperature profiles for the axial and lateral direction of the combustion chamber and a detail of the baseplate from the experiments are shown in Fig. 5. At the outlet of the chimney, an outflow boundary condition is imposed. Here, velocity and all transport equations are extrapolated whereas the pressure is fixed to atmospheric conditions.

A constant time step $\Delta t = 5 \times 10^{-6}$ s is set ensuring CFL numbers below unity. For all cases, the simulation is initialized over $\tau_{init} = 0.1$ s before temporal statistics are collected over consecutive $\tau_{avg} = 0.1$ s. This is based on an estimation of the mean residence time $\overline{\tau}_{res} \approx 0.005$ s inside the combustor and previous test simulations which analyzed the convergence of statistical moments in the gaseous and the dispersed phase during averaging.

4.3 Spray Boundary Condition from the PAMELA Model

The PAMELA primary breakup model as detailed in Sect. 2.2.2 is used for the definition of the spray boundary condition. Droplets start from an annulus with $r_i = 3.5$ mm and $r_o = 4.5$ mm, placed at an axial offset $\Delta z = 1.5$ mm with respect to the atomizer edge. The PAMELA model provides an SMD D_{32} and a spread factor q for a Rosin-Rammler distribution as defined in Eq. (5). Inputs to the model are the atomizer edge thickness h_a, the length of the liquid film L_f along the prefilmer and the mean gas velocity U_G parallel to the liquid film.

For the SSB, the atomizer edge thickness is reported as $h_{a,SSB} = 0.1$ mm Grohmann (2019). Based on the geometry of the prefilmer (see right part of Fig. 3) and the nominal opening angle of the primary pressure-swirl atomizer ($\theta = 60°$), the location where droplets from the primary atomizer impinge the prefilmer surface can be reconstructed and hence the liquid film length estimated as $L_{f,SSB} = 3.8$ mm. Mean gas velocity $U_{G,SSB}$ alongside the liquid film is extracted from preliminary simulations of the mean gas field and ranges between 70 and 85 ms^{-1} as the air flow is accelerated within the inner air nozzle.

Fig. 6 Definition of the velocity vector $\vec{U}_D$ at the spray boundary condition. Black system: Global coordinate system. Green system: Local coordinate system. Blue dots: Droplet starting annulus
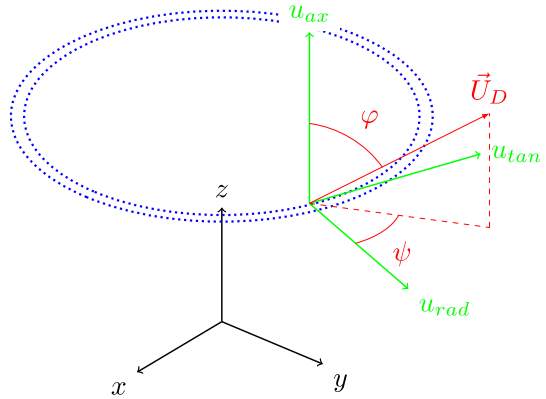
The PAMELA model does not provide data for the velocity components of the droplets after primary atomization. Therefore, it is assumed that the droplets rapidly couple to the local gas flow at the starting annulus. This is supported by findings from previous simulations. It was found that close to the starting annulus, most droplets had a Stokes number below 10. Therefore, the velocity vector $\vec{U}_D$ of a droplet starting at the boundary condition is derived from the local vector of the gas velocity. The definition of $\vec{U}_D$ is depicted in Fig. 6: In the local polar coordinate system of the droplet, $\vec{U}_D$ is determined by the axial angle φ_D, the swirl angle ψ_D and the velocity magnitude U_D.

4.4 Identification of Input Uncertainties

Sources of uncertainties are identified by analyzing the simulation model for the SSB with respect to input uncertainties. They might arise from uncertainties in the geometry, the modeling constants, as well as boundary conditions for the continuous and dispersed phases.

4.4.1 Geometry

All geometric dimensions and quantities of the SSB, e.g. the combustor length or the dimensions of the channels in the swirler, are documented in the work of Grohmann (2019). Furthermore, the reduced complexity of the geometry in comparison to a full-scale aero-engine enables the resolution of all geometric features in the computational grid.

The atomizer edge thickness h_a serves as an input to the primary atomization model. As detailed in Sect. 4.3, this parameter is known for the SSB. In a preliminary study using the PAMELA model, uncertainties within the reported manufacturing tolerance have shown to have no significant effect on the droplet size distribution calculated by the PAMELA model. For example, the SMD varied by $\pm 1\%$ due to $h_a = 0.1 \pm 0.05$ mm, which is the reported manufacturing tolerance for h_a.

4.4.2 Modeling Constants

The simulation case under consideration involves a number of sub-models and thus numerous modeling constants which might affect the simulation results. For example,

the choice of the Smagorinsky constant C_s in the SAS turbulence model influences the turbulent damping in the LES regions (Ivanova 2012).

In the present study, all modeling constants are set to their respective reference values for which they were validated. This includes modeling constants for the CTM vaporization model, the hybrid turbulence model and the PAMELA primary breakup model. Since uncertainties in modeling constants are beyond the scope of this study, impact of uncertainties in these parameters are not further investigated.

4.4.3 Initial and Boundary Conditions of the Gas Phase

Regarding the boundary condition for the gaseous phase, a simplification applies to the inlet at the plenum, at which the turbulence intensity I_t was not measured in the experiments. Therefore, a uniform inlet velocity rather than synthetic turbulence (Klein and Sadiki 2003) is imposed. In view of the fact that the flow undergoes a strong contraction and most of the turbulence is generated in the swirler stages, this uncertainty should not affect the flow inside the combustion chamber. Measurement uncertainties below 1.2% have been reported for the mass flow rate of the air (Grohmann 2019).

Mercier and Schmitt (2015) demonstrated that uncertainties in wall temperatures and associated heat losses can have a significant impact on local and global temperature distribution. In the present study, temperature profiles from thermometry measurements are utilized. For this data, Grohmann (2019) estimated an error of $\pm 2\%$.

4.4.4 Initial and Boundary Conditions of the Dispersed Phase

Since the velocity vector of the droplets at the dispersed phase boundary condition is derived from the gas field trajectories, uncertainties are introduced from the variation of the trajectory angle ψ and φ over the starting annulus. In the flow field, ψ ranges between 55° and 63° while φ varies between 26° and 29°. Furthermore, by applying the absolute velocity $U \approx 60 \text{ ms}^{-1}$ of the gas phase at the starting annulus to the dispersed phase, droplets start with a significantly too high momentum and mostly impinge at the combustion chamber walls. Therefore, the droplets' absolute velocity U_D is assumed to be between 25 and 30 ms^{-1}. This is inferred from similar atomizer configurations (Setzwein et al. 2019; Jones and Marquis 2014). As mentioned in the previous section, the mean gas velocity U_G alongside the liquid film ranges between 70 and 80 ms^{-1}.

Finally, uncertainties exist regarding the temperature of the liquid droplets at the boundary condition. In the experiments, the temperature of the fuel in the supply system was measured at a location close to the primary pressure-swirl atomizer ($T_{liq,exp} = 303$ K). However, the fuel might undergo additional heating during pre-filming atomization due to the surrounding air flow ($T_{air} = 323$ K) as well as radiative heat transfer from the reaction zone. Accordingly, the droplets' temperature is estimated to range between $T_{liq,exp} = 303$ K and $T_{air} = 323$ K.

Table 3 provides an overview of the most relevant sources of input uncertainties as identified in this section. Note that depending on the scope of the analysis, additional quantities could be included.

Table 3 Relevant sources of input uncertainties in the simulation model

	Quantity	Value	Unit	Description
Geometry				
	h_a	0.1 ± 0.05	[mm]	Atomizer edge thickness
Modeling constants				
	C_s	0.145	[−]	Smagorinsky constant
BC gas phase				
	I_t	Not reported	[−]	Turbulence intensity
	$\dot{m}_{air}$	$4.3 \times 10^{-3} \pm 1.2\%$	[kg/s]	Air mass flow rate
	T_{wall}	$T(x, y, z) \pm 2\%$	[K]	Wall temperature
BC dispersed phase				
	φ_D	[26, 29]	[°]	Droplet axial angle
	ψ_D	[55, 63]	[°]	Droplet swirl angle
	U_D	[25, 30]	[ms^{-1}]	Droplet absolute velocity
	U_G	[70, 85]	[ms^{-1}]	Mean gas velocity
	T_{liq}	[303, 320]	[K]	Droplet liquid temperature

4.5 Probabilistic Modeling and PCE Construction

From the possible uncertainties identified in the previous section, only the uncertainties in the spray boundary condition will be analyzed in detail, since these parameters play a key role in the early stage design process of novel combustor systems. In a previous study (Enderle and Rauch 2020), uncertainties in the spray boundary condition demonstrated a significant effect on the flame position and temperature distribution over the reaction zone. Thus, the input parameters to the PAMELA model are seen as uncertain inputs to the simulation model.

For simplicity, they are all interpreted as uncorrelated uncertainties and characterized by a joint uniform distribution function with the respective minimum and maximum from the previous analysis. The choice of uniform distribution functions for the marginal distributions in case of minimum/maximum data is derived from the principle of maximum entropy (Kapur and Kesavan 1992; Sudret 2007). Thus, precise probability theory is applied, resulting in a probabilistic simulation model of the SSB, enabling insight into the probabilistic structure of the uncertainties in the simulation results. Table 4 provides a summary of the uncertain input parameters which form the input space $\Omega_{SSB} = [\varphi_D \times \psi_D \times U_D \times U_G \times T_{liq}]$. Note that the uncertainty in the mean gas

Table 4 Parameter space Ω_{SSB} of the input uncertainties

	Description	marginal PDF	Unit	Source
φ_D	Axial angle	$\mathcal{U}(26, 29)$	[°]	CFD flow field
ψ_D	Swirl angle	$\mathcal{U}(55, 63)$	[°]	CFD flow field
U_D	Absolute velocity	$\mathcal{U}(25, 30)$	[ms^{-1}]	Estimated
U_G	Mean gas velocity	$\mathcal{U}(70, 85)$	[ms^{-1}]	CFD flow field
T_{liq}	Liquid temperature	$\mathcal{U}(303, 320)$	[K]	Grohmann (2019)

velocity U_G results in SMDs $D_{32} = 29 - 35$ μm and MMDs $D_{50} = 35 - 41$ μm calculated by the PAMELA model.

Output uncertainties in the probabilistic simulation model are quantified through PCE. The present study specifically focuses on gas phase temperature as quantity of interest, since its accurate prediction plays a crucial role in combustor design (Lefebvre 2010). However, additional quantities of interest from the gas phase as well as the dispersed phase are considered in order to get insight into the phase-coupling dynamics under the given uncertainties. Formally, the truncated PC expansion of a Quantity of Interest Q from the probabilistic simulation model reads:

$$Q = \sum_{k=0}^{P} \alpha_k \boldsymbol{\Psi}_k(\boldsymbol{\xi}) = \sum_{k=0}^{P} \alpha_k \boldsymbol{\Psi}_k \left(\xi_{\varphi_D}, \xi_{\psi_D}, \xi_{U_D}, \xi_{U_G}, \xi_{T_{liq}} \right). \tag{24}$$

Since all uncertainties in Table 4 follow a uniform distribution function, Legendre polynomials form the basis $\boldsymbol{\Psi}_k$ (Xiu and Karniadakis 2002). Multidimensional integration on a Smolyak sparse grid is utilized for the computation of series coefficients α_k. A Level-2 expansion is considered, requiring 71 evaluations of the simulation model. The distribution of the integration points over the the parameter space Ω_{SSB} is shown exemplarily for the φ_D subspace in Fig. 7. Since a single model evaluation requires approximately 22000 CPU hours, the total computational cost for this study is in the order of 1.5×10^6 CPU hours.

The fact that precise distribution functions are assigned to all input uncertainties allows for a computation of probability distribution functions for the Quantities of Interest from space filling sampling of Ω_{SSB}. For this purpose, 10^5 samples are drawn from the respective PC expansion.

4.6 Results and Discussion

4.6.1 Cold Flow Validation

In order to validate the modeling setup, a deterministic simulation of the cold flow is conducted. Only main features for which experimental data is available are discussed.
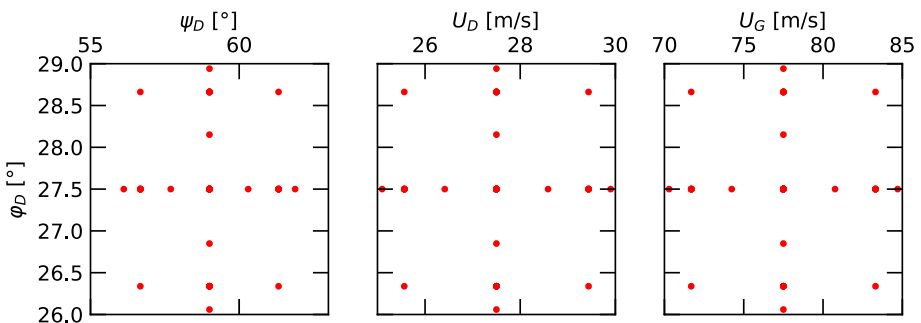
Fig. 7 Level-2 PCE quadrature points (
■) of a Smolyak sparse grid over the parameter space Ω_{SSB} using a Gauss-Patterson rule

For a thorough analysis of the SSB baseline case, the reader is referred to the work of Eckel (2018) and Grohmann (2019).

Since the quality of Scale Adaptive Simulations strongly depends on the ability of the grid to locally resolve turbulent fluctuations and thereby switch into LES mode, the local spatial resolution must be reassessed for each problem under consideration. For this purpose, a first criterion is given by the ratio r_k of resolved to total turbulent kinetic energy. It is defined as

$$r_k = \frac{\overline{k}_{res.}}{\overline{k}_{res.} + \overline{k}_{mod.}} = \frac{\frac{1}{2}\overline{u_i'u_i'}}{\frac{1}{2}\overline{u_i'u_i'} + \overline{k}_{mod}},$$

(25)

where $\overline{u_i'u_i'}$ denotes the time-averaged product of velocity fluctuations u_i', whereas $\overline{k}_{mod}$ is the modeled turbulent kinetic energy from the SST turbulence model. According to Pope (2004), in a well-resolved LES this ratio should be at least 0.8, meaning that 80% of the local turbulent kinetic energy budget is being resolved. The criterion is satisfied for the most parts of the computational domain, with exception of the inlet plenum and the swirler vanes, where a URANS solution is obtained.

As a further criterion, the ratio of turbulent to molecular viscosity $r_\mu = \overline{\mu_t}/\overline{\mu}$ is calculated. In LES regions, this ratio should not exceed $\mathcal{O}(10^1)$ (Ivanova 2012; Menter 2012). Similar to the turbulent kinetic energy criterion this is not the case for the core region of the air nozzle, whereas in the combustion chamber, the criterion is met.

(a) Instantaneous   (b) Time-averaged
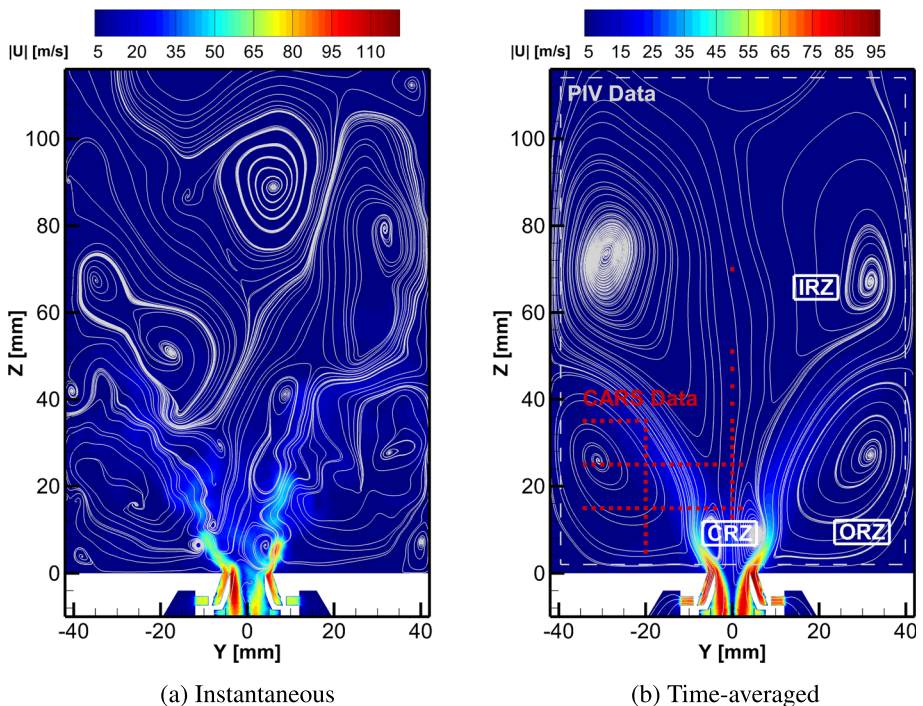
Fig. 8 Simulation results for absolute velocity and streamtraces of the non-reacting flow field

An overview of the structure of the non-reacting flow field is given in Fig. 8 by means of contours of absolute velocity in the central $y-z$ plane. In the transient snapshot (Fig. 8a), highest velocities are found inside the air nozzle, specifically at the nozzle exit where the flow reaches a maximum of $|U|_{max} \approx 120$ ms^{-1}. This corresponds to a local Mach number of Ma ≈ 0.34 which is close to the limit of the incompressibility assumption (Poinsot and Veynante 2005). The superimposed streamlines (gray lines) display a strongly turbulent and three-dimensional flow field with vortices shedding from the shear layer caused by the high local velocities at the exit of the air nozzle.

Figure 8b displays the flow field averaged over the simulation runtime. Flow patterns typical for confined swirling flows (Lucca-Negro and O'Doherty 2001) are observable: A small central recirculation zone (CRZ) is formed around $z = 0$ mm reducing the effective outflow area of the inner nozzle. As a consequence, velocity is increased along the pre-filmer. Furthermore, a negative pressure gradient along the z-axis causes a backflow and thus a large inner recirculation zone (IRZ) with a stagnation point at $z \approx 110$ mm. Finally, the back-pressure of the walls and the strong shear layer from the air nozzle establish a counter-rotating outer recirculation zone (ORZ).

Radial profiles of the velocity components from PIV enable a quantitative validation of the simulation results. Figure 8b indicates the region for which PIV data is available in the $y-z$ plane. A comparison of the time-averaged axial velocity and the respective RMS fluctuation is given in Fig. 9 by means of profiles along the lateral y-axis. Axial positions between $z = 5$ mm and 40 mm are considered as this region contains the main reaction zone in the following simulation of the reacting flow. For the mean velocity $\overline{w}$, simulation and experiment are in excellent agreement regarding magnitude and radial distribution. As aforementioned, a backflow along the z-axis ($y = 0$ mm) is visible. Regarding fluctuations $\overline{w'}$, the simulation overestimates the fluctuation intensity, specifically at $z = 5$ mm, $z = 10$ mm and $z = 20$ mm. Note that for the simulation, the displayed fluctuation is the total budget of resolved and modeled fluctuations:
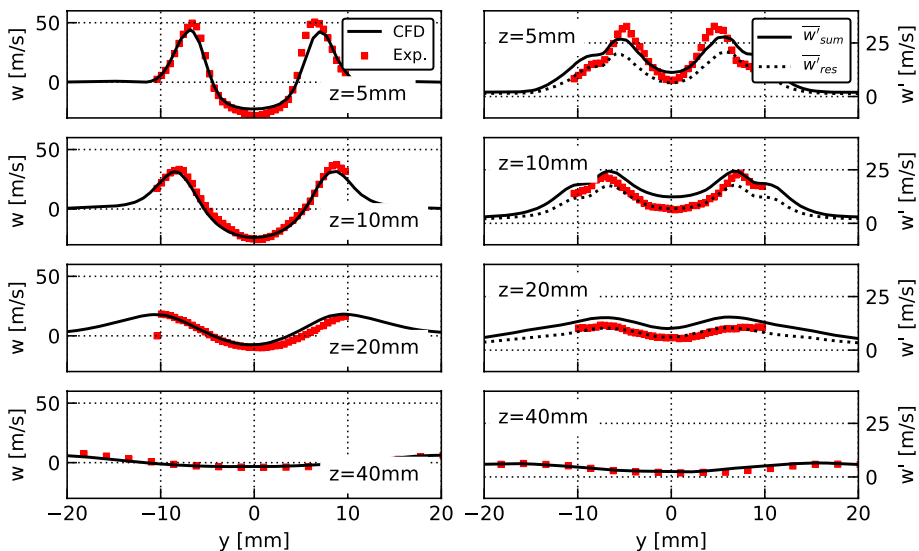
Fig. 9 Time-averaged profiles of axial (w) velocity component at different axial positions from cold flow measurements and simulation. Mean (left column) and RMS (right column)

$$\overline{w'}_{sum} = \overline{w'}_{res} + \overline{w'}_{mod} = \overline{w'}_{res} + \sqrt{\frac{2}{3}\overline{k}_{mod}}. \tag{26}$$

Thus, the overestimation could be a potential imbalance between resolved and modeled fluctuations as a result of the transition from URANS to LES mode of the SAS model, which was identified in the previous section, especially since the resolved part of the fluctuations agrees well with the experimental data.

Further comparison between experiment and simulation is shown in Figs. 20 and 21 in the appendix for the v and u velocity components, respectively. Again, mean data is accurately reproduced by the simulation, while fluctuations are slightly too low, especially at the first axial position.

From the inspection of the two criteria r_k and r_μ as well as the comparison with PIV data for the flow field, it is concluded that the spatial resolution of the simulation setup is sufficient for a Scale Adaptive Simulation of the SSB.

4.6.2 Reacting Flow Under Uncertainties—Gas Phase

At first, a single realization from the probabilistic simulation model is considered to provide an overview of the combustion process. For this purpose, the central point of the PC expansion over Ω_{SSB} with $\varphi_D = 22.5\,°, \psi_D = 59\,°, U_D = 27.5\,\mathrm{ms}^{-1}, U_G = 77.5\,\mathrm{ms}^{-1}, T_{liq} = 311.5\,\mathrm{K}$ is analyzed. An impression of the combustion process is given by means of contours of gas

(a) Instantaneous (b) Time-averaged
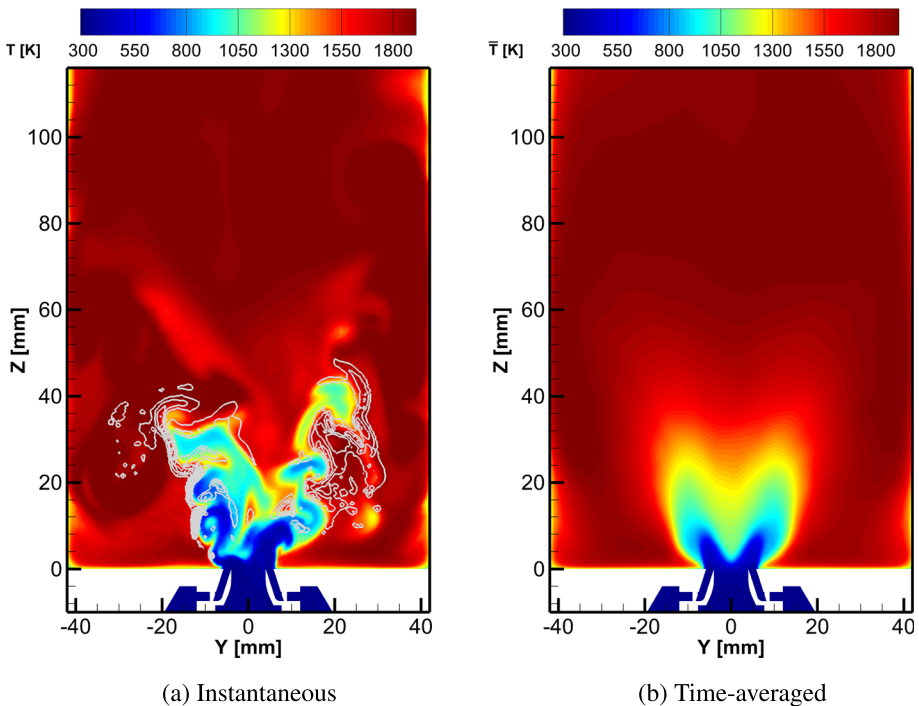
Fig. 10 Deterministic simulation results for gas phase temperature of the reacting flow field at the central point of Ω_{SSB}. Gray lines indicate heat release

phase temperature in Fig. 10. The transient snapshot in Fig. 10a shows a wrinkled flame front, indicated by gray contour lines of heat release. In this flame front, fuel that has been transferred to the gas phase is consumed and local temperature increases significantly. The reaction zone extends from $z = 5$ mm up to $z = 40$ mm. Hot gases from the flame front accumulate in the outer recirculation zone and are partly transported back to the centerline by large eddies from the inner recirculation. Close to the exit of the air nozzle, these hot gases mix with the cold air flow. With increasing axial distance from the reaction zone, the temperature field becomes more homogeneous. Maximum temperature ranges in the magnitude of $T_{max} = 2000$ K which is well below the theoretical maximum temperature $T_{max}^{adi} \approx 2250$ K in case of an adiabatic equilibrium. To further illustrate the influence of heat losses due to the isothermal walls and the influence of finite rate chemistry, Fig. 11 displays the different states of the reacting system in the mixture fraction - temperature space. Each scatter represents a positions within the computational domain with its respective mixture fraction Z and transient temperature T. Scatter color corresponds to the axial position. The black line represents the limit of infinitely fast chemistry under adiabatic conditions calculated by an adiabatic equilibrium computation with CANTERA (Goodwin et al. 2018). This limit cannot be reached as the system suffers from heat losses at the isothermal walls. Instead, an upper limit is found approximately 250 K below the adiabatic limit (gray line). This new upper limit can be met in the equilibrium computation with CANTERA by reducing the thermal input by 1.75 kW or 17%. This value can be seen as an approximation of the heat loss due to the isothermal walls. As also evident from Fig. 11, a significant number of states in the main reaction zone (red and purple dots) deviate from the gray equilibrium line, indicating that these states are governed by a finite rate
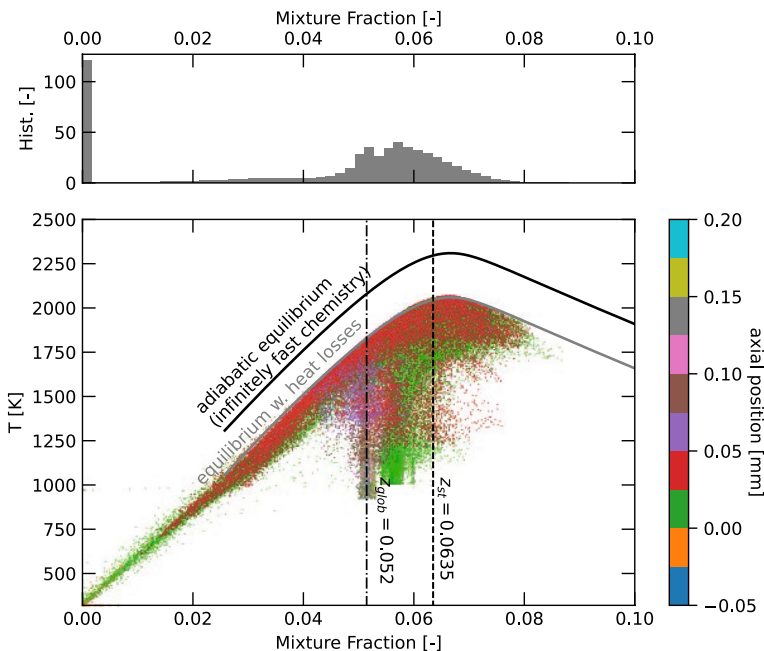

Fig. 11 Transient state of the reacting multiphase flow characterized by mixture fraction and temperature. Colors indicate axial position

chemistry. In such states, fuel and oxidizer can coexist since the diffusion and flow time-scales are significantly larger than the chemical timescales.

In the time-averaged field of gas phase temperature (Fig. 10b), an M-shaped cold inner zone with axially increasing temperature is visible as well as local hot spots in the outer recirculation zone. In the vicinity of the walls, the influence of the isothermal boundary condition is observable.

In the following, probabilistic results from space filling sampling of the PC expansion over Ω_{SSB} are taken into consideration. Hence, the full probabilistic strucuture of all quanti-ties of interest can be investigated. Gas phase temperature from the probabilistic simulation is investigated by means of axial and radial profiles over the combustion chamber in the $y - z$ plane, following the CARS measurement locations as indicated in Fig. 8b. Result-ing temperature profiles from the PCE over Ω_{SSB} are shown in Fig. 12a–e. The probability structure of the uncertain simulation results is characterized by probability intervals: light gray areas indicate regions with $5\% < \Pr(T) < 95\%$, whereas dark gray areas represent $25\% < \Pr(T) < 75\%$. The median realization is given by cyan lines. Red squares show the mean temperature $\mu(T_{exp})$ from the CARS measurements while the error bars indicate the corresponding standard deviation $\sigma(T_{exp})$. Most notably, the probability intervals clearly
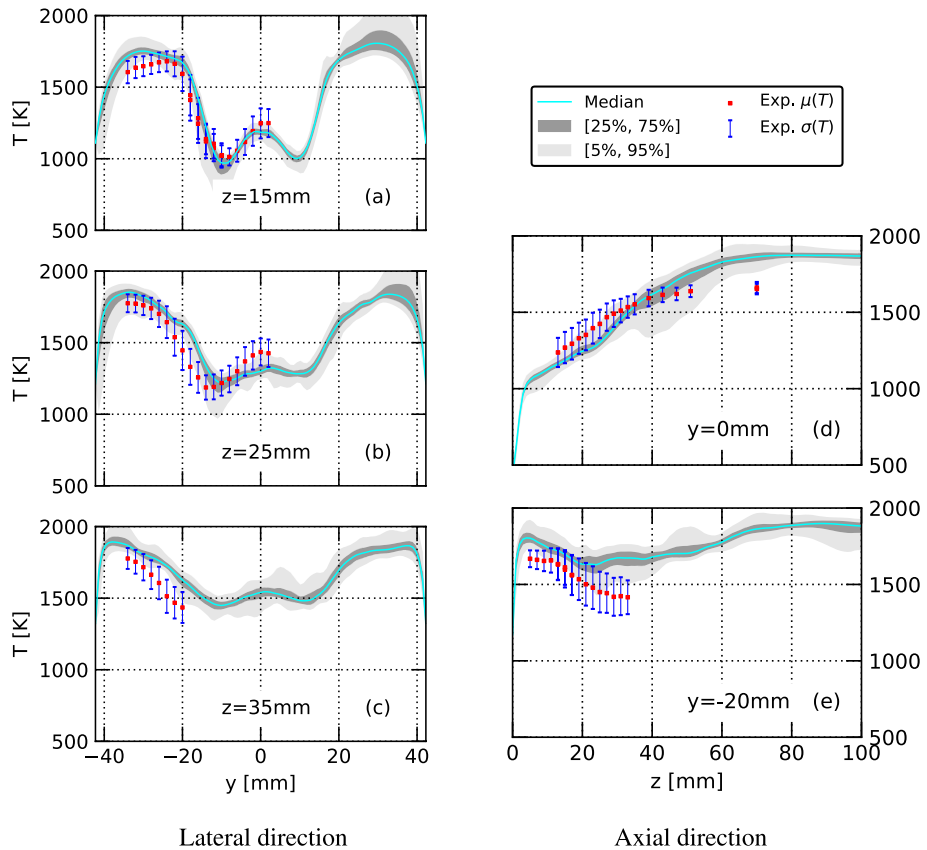
Fig. 12 Non-deterministic simulation results for time-averaged profiles of gas phase temperature. Error bars (⎯) indicate standard deviation of the experimental measurements

reveal a non-uniform distribution of output uncertainties, despite the fact that all input uncertainties were defined as uniformly distributed. This highlights the non-linear propagation of uncertainties through the simulation model.

Over all positions, moderate uncertainties in the magnitude of $100-200$ K regarding the [5%;95%] intervals are visible. In the z-profiles (Fig. 12d, e), highest uncertainties are located at the high temperature regions ($y \approx \pm 30$ mm) where most of the combustion reactions take place. These processes are closely connected to the supply of fuel components through spray evaporation, which is ultimately linked to the input uncertainties at the spray boundary conditions. At the first two axial positions, the non-deterministic simulation is able to bracket almost all experimental data. However, at $z = 35$ mm (Fig. 12c) the temperature profile is still overestimated in the simulation results.

Although the spray boundary condition is symmetric with respect to the z-axis, the uncertain simulation results in the z-profiles appear slightly asymmetric, especially regarding the [5%;95%] intervals. This could be caused by noisy data for the construction of the PCE due to incomplete time-averaging in the numerical simulation, insufficient PCE accuracy or an insufficient sample size for the precise computation of the local PDF. Since the influence of time-averaging was investigated in detail for the reference simulation, the asymmetry is most likely due to local PCE accuracy. In Enderle and Rauch (2020) it was identified that the quality of the PC expansion can vary along a profile of QoIs for a complex simulation problem.

Along the axial profile at $y = 0$ mm (Fig. 12d), all measurement data except for the last one are included in the uncertainty region. However, the fact that the axial gradient in the experimental data is almost zero over the last few measurement positions whereas the temperature in the simulation still rises up to 1800 K indicates that the temperature in the upper half of the combustor is systematically overestimated in the simulation. This could be caused by deficient thermal losses at the combustor walls due to the thermal boundary condition. Furthermore, it could also stem from a general modeling error.

A significant increase in local uncertainty in the $y = 0$ mm profile (Fig. 12d) is found between $z = 40$ and $z = 80$ mm. This coincides with the axial position of possible spray-wall impingement after which the droplets are reflected back towards the centerline region. Presumably, this impingement depends on the droplets' starting velocity U_D and their axial angle φ_D. Hence, uncertainties in these quantities might influence the spray impingement location and finally the temperature profiles downstream of the respective location.

The tendency in the z-profiles that highest uncertainties are found in the high temperature regions is also reflected in the $y = -20$ mm profile (Fig. 12e). Here, the mean of the experimental data is within or below the 5% quantile at all positions.

For a quantitative comparison of the non-deterministic simulations and the experimental data, the accuracy metrics *Continous Rankend Probabilty Score* (CRPS) from Eq. (21) and *Wasserstein-1* (W_1) from Eq. (22) are calculated. In the calculation of the CRPS, the mean of the experimental data μ_{exp} at each location is interpreted as a *certain* observation. The CRPS yields a generalized mean absolute error in case of uncertain predictions and certain experimental observation. Thus, the measurement error from the experiment is not taken into account and the CRPS is calculated from the local cumulative distribution function of the temperature from the non-deterministic simulation and the mean temperature from the experiment. The local CRPS for the temperature predictions from the non-deterministic simulation is given in Fig. 13a–e. Note that the CRPS is only calculated at radial and axial positions for which experimental data is available. In order to compare the probability structure of the non-deterministic simulation results and the experimental data including measurement errors, the Wasserstein-1 metric for
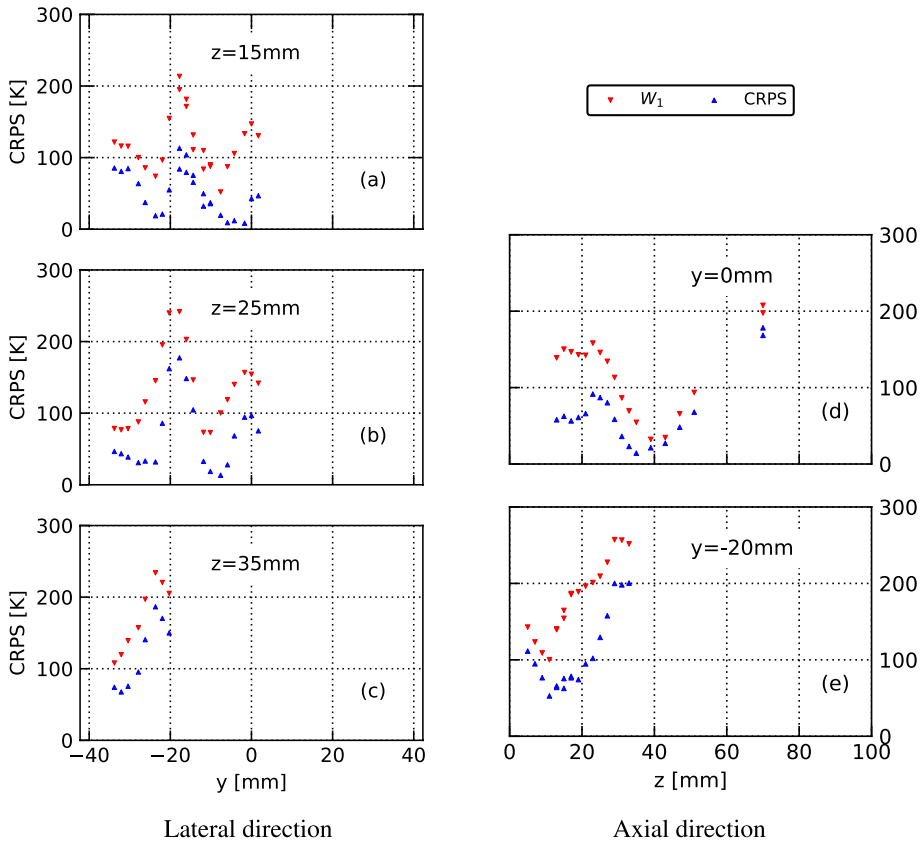
Fig. 13 CRPS (■) and Wasserstein metric W_1 (■) for the probabilistic temperature predictions

the temperature results is calculated at the same positions as the CRPS. For this purpose, the measurement uncertainty and hence the uncertain observation is assumed to follow a normal distribution $\mathcal{N}(\mu_{exp}, \sigma_{exp})$. The standard deviation σ_{exp} is available from the experimental database Cantu and Grohmann (2018). Results for W_1 are also included in Fig. 13a–e. At all positions, $W_1 >$ CRPS stemming from the fact that W_1 compares the full probability structure of experiment and simulations, thereby including additional degrees of freedom compared to the point estimate in the CRPS. Key findings from the previous qualitative comparison are confirmed by the metrics: highest values for both metrics, and therefore highest uncertainties, are found around $y = -20$ mm and $y = 0$ mm for the radial profiles. Uncertainties in the simulation results increase along the axial profile. The mean absolute error under uncertainties given by the CRPS stays between 50 K and 200 K at all positions. The observation that W1 greatly exceeds CRPS at certain positions, such as $y = -20$ mm, $z = 20$ mm in Fig. 13e, implies that these positions not only exhibit an absolute deviation between the experimental and uncertain simulation results, but also a substantial disparity in the probability distribution's shape.

Results for the axial component of gas phase velocity in Fig. 14a–e demonstrate that uncertainties in the temperature distribution couple with uncertainties in the gas phase velocity. As in the temperature profiles, highest uncertainties in the z-profiles are found
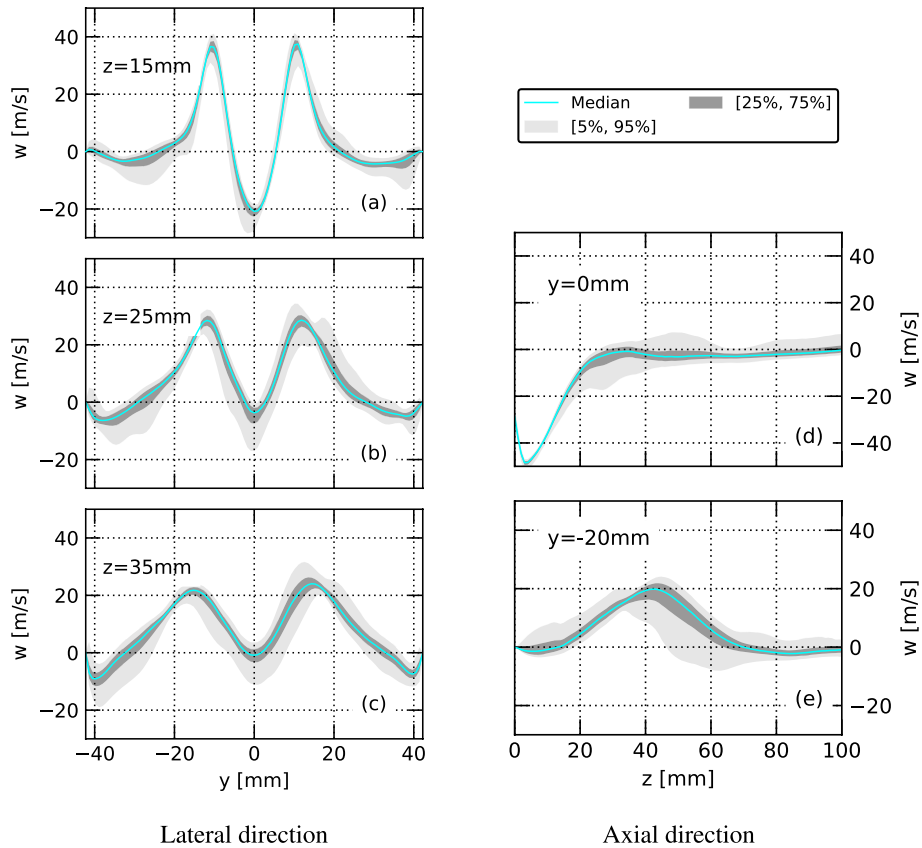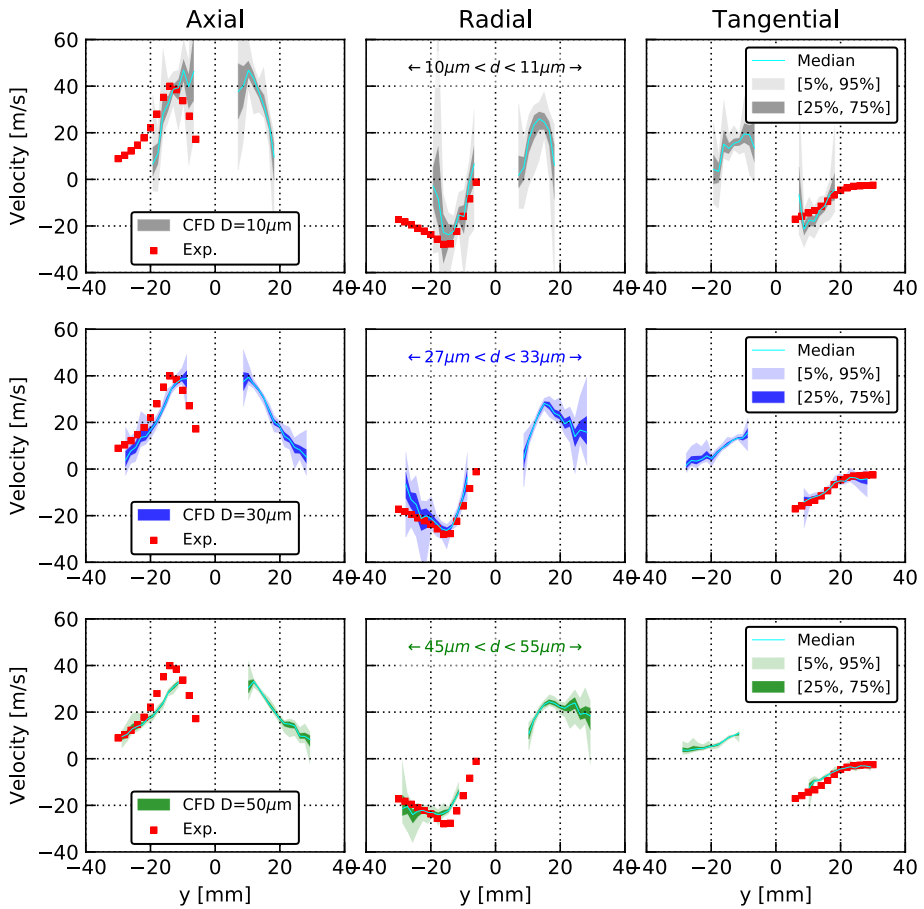
Fig. 14 Non-deterministic simulation results for time-averaged profiles of axial velocity in the gas phase

around the reaction zone. Moreover, the width of the [5%, 95%] interval increases with increasing axial distance. This tendency is also present in the axial profiles ($y = 0$ mm, $y = -20$ mm; Fig. 14d–e) and might be an indicator that the backflow of hot combustion products is affected by the variations in the temperature field due to the input uncertainties with respect to the spray boundary condition. Since experimental data for the velocity field in the reacting flow is not available, a final statement wether the varations in the velocity field are mainly driven by the input uncertainties or an amplification of the effect of general modeling choices is prohibitive.

4.6.3 Reacting Flow Under Uncertainties—Dispersed Phase

Statistics of the dispersed phase are collected in a two-dimensional registration plane at $z = 15$ mm which is parallel to the $x - y$ plane. Hence, particles from the dispersed phase passing through the registration plane are registered with its respective properties (e.g. velocity, diameter) and time-averaged over the simulation runtime using a cartesian grid over the registration plane for spatial discretization. For each quantity of interest (e.g.

Fig. 15 Non-deterministic simulation results for time averaged profiles of droplet velocity components at $z = 15$ mm. Simulation data is split into small (■), medium (■), and large droplets (■). Experimental data (■) is averaged over all diameters

droplet velocity components, liquid volume flux) a PCE is then constructed and sampled over Ω_{SSB} as decscribed in Sect. 4.5. Figure 15 provides a comparison between the non-deterministic results and PDA data (experiment). The three velocity components are defined with respect to the global coordinate system. Thus, the axial, radial and tangential velocity is derived from the global z, y and x velocity, respectively. The droplets experience a swirling motion in the mathematical positive direction with respect to the z-axis, as they couple to the gas flow. Droplet data from the probabilistic simulation is subdivided into three distinct diameters (10, 30, 50 μm) to display the droplet dispersion. A $\pm 10\%$ margin is added for a better statistical convergence. Therefore, the three size classes are defined as 10 μm $< d <$ 11 μm (*small*), 27 μm $< d <$ 33 μm (*medium*), and 45 μm $< d <$ 55 μm (*large*). In contrast, from the PDA measurements only averaged data regarding the droplet

diameter is available. Note that probabilistic simulation results are only shown for locations at which sufficient time-averaged droplet data is available from all 71 simulations. Otherwise, the PC expansion would be prone to high local approximation errors. As for the temperature profiles, the probability structure is characterized by the two probability intervals [5%;95%] and [25%;75%] as well as the median realization.

Despite the fact that all input uncertainties from Table 4 are directly linked to the dispersed phase, output uncertainties in the components of droplet velocity are low, especially for the medium (blue) and large (green) droplets. The fact that the magnitude of uncertainty increases towards lower droplet diameters can be explained by their low Stokes number and thus higher tendencies to couple to the local gas velocity. As aforementioned, output uncertainties are also present in the velocity components of the gas field. Hence, these uncertainties might be passed on to the small droplets. In contrast, uncertainties in the velocity components of the large droplets simply reflect the input uncertainty in the absolute velocity U_D of 5 ms^{-1}.

In general, magnitude and profile of the velocity components are well reproduced by the probabilistic simulation. A slight dispersion in axial velocity is observable over the three size classes. Overall, the probabilistic simulation results for the droplet velocity verify the assumption made in the definition of the spray boundary condition that the droplet starting trajectories can be derived from the local gas velocities.

Figure 16 provides probabilistic simulation results for Sauter Mean Diameter and normalized liquid volume flux through the registration plane at $z = 15$ mm. Although experimental data for the SMD ranges between 17 µm and 32 µm, the probabilistic simulation predicts a maximum SMD in the magnitude of 40 µm and a minimum below 15 µm. However, the SMD profiles must be interpreted with respect to the volume flux data for which simulation and experiment are in good agreement and uncertainties in the simulation are low (see Fig. 16a). Close to the z-axis ($y = 0$ mm), the SMD in the simulation reaches its minimum while the volume flux drops to almost zero. Therefore, these droplets relate

(a) SMD   (b) liquid volume flux
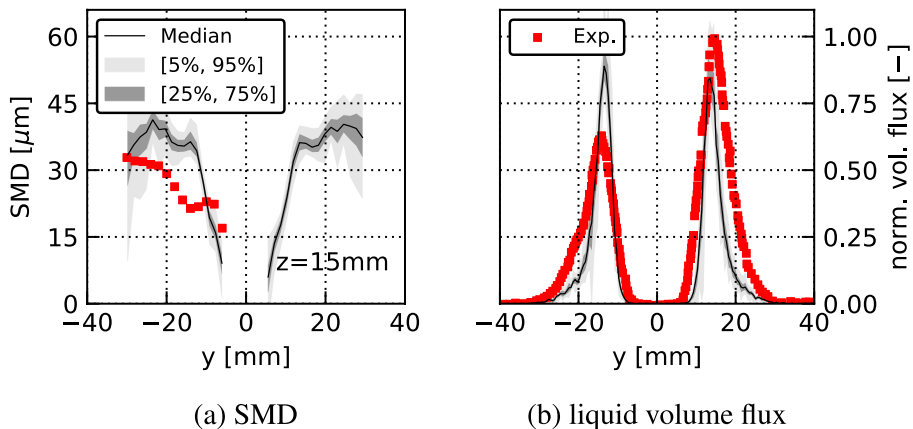
Fig. 16 Non-deterministic simulation results for time averaged profiles of Sauter Mean Diameter (SMD) and normalized liquid volume flux at $z = 15$ mm

to a very low volume flux. In contrast, at the radial position of maximum volume flux ($y \approx \pm 17.5$ mm) the uncertainty level with respect to the [5%;95%] interval is in the magnitude of 5 μm which is the range of SMDs provided by the PAMELA model under the given uncertainty for U_G. The radial position of maximum volume flux in Fig. 16b appears almost unaffected by the input uncertainties, confirming that the distribution of droplets is dominated by the gas field in the SSB case.

For brevity, additional plots for droplet velocities and mean diameter at $z = 25$ mm are given in Figs. 22 and 23 in the appendix. Similar phenomena and tendencies as discussed for $z = 15$ mm can be identified.

4.6.4 Reacting Flow Under Uncertainties—Reaction Zone

Insight into the probability structure of integral quantities of interest under the given uncertainties is provided by the examples of mean flame lift-off height h_{LO} and mean flame length L_F, since most other quantities are highly correlated with the location of the reaction zone in the combustor. Both quantities are derived from the line-of-sight (here: y-axis) integrated and time-averaged OH* concentration in the $\overline{Y}_{OH^*}$ simulations, as the OH* radical is primarily found in the reaction zone. Therefore, h_{LO} is defined as the mean axial distance between the contour $v \cdot \max(\overline{Y}_{OH^*})$ and the exit plane of the air nozzle, while l_F is defined as the difference between the mean extent of this contour minus h_{LO}. In this definition, v is a threshold value which is set to 70%. A depiction of the parameters' definition is available from Fig. 17a–c.

Figure 18 summarizes results from space filling sampling of the PCE over Ω_{SSB} through histograms and the corresponding empirical CDFs $\hat{\mathscr{C}}_{L_F}$ and $\hat{\mathscr{C}}_{h_{LO}}$. As evident from the histograms, both QoIs follow a distribution function that resembles a normal distribution, despite the fact that all input uncertainties are uniformly distributed. As already discussed for the temperature profiles, this points out that the flame stabilization in the SSB follows a highly non-linear mechanism regarding the injection of liquid fuel droplets.

(a) Transient OH* distribution   (b) Time averaged OH* distribution   (c) Definition of h_{LO} and l_F
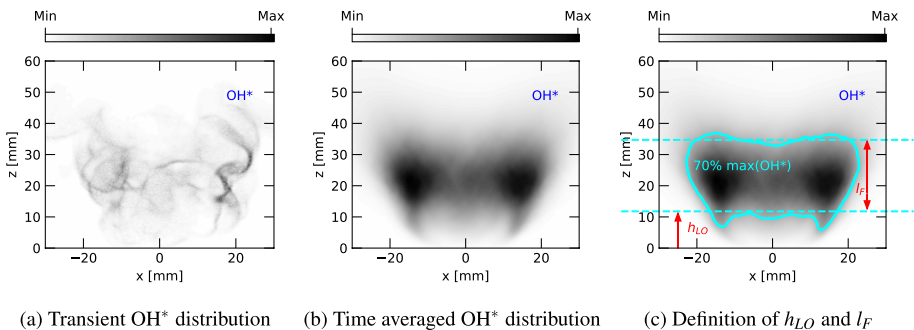
Fig. 17 Definition and extraction of flame lift-off height h_{LO} and flame length l_F from line of sight intergrated OH* simulation results
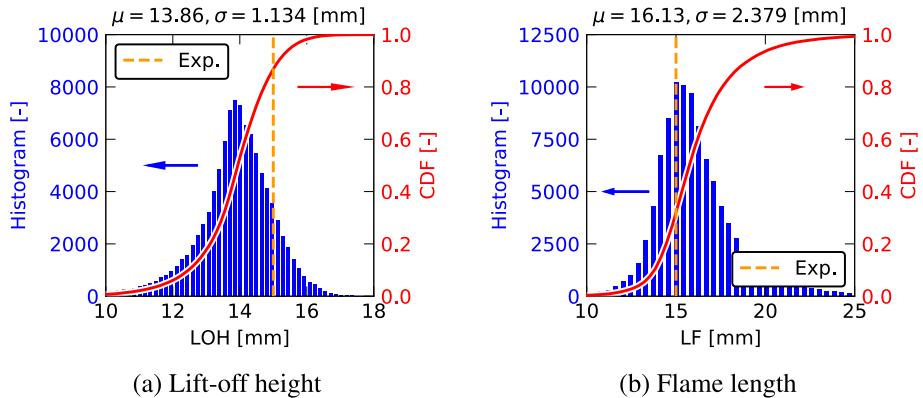
**Fig. 18** Non-deterministic simulation results for flame lift-off height and flame length with respect to a threshold value $\upsilon = 50\%$

Experimental results are indicated by orange dashed lines. In case of L_F (Fig. 18b), the experimental value coincides with the *mode* of $\hat{\mathscr{P}}_{L_F}$, i.e. the most probable realization from the simulation. This should not be confused with the *mean* realization $\mu_{L_F} = 16$ mm, which is greater than the experimental value. Regarding h_{LO} most realizations underestimate the true lift-off height from the experiment (Fig. 18a). From $\hat{\mathscr{C}}_{h_{LO}}$ it can be inferred that 80% of the realizations are below the experimental value.

To asses the sensitivity of the two global flame parameters h_{LO} and L_F to the uncertainties in the input parameters, Sobol' indices are derived from the Polynomial Chaos Expansion. Figure 19 summarizes the first order Sobol' indices $S_{1,i}$ and total Sobol' indices S_i^T with respect to the five uncertain input parameters. Note that total order indices are indicated by hatched color bars.

The flame lift-off height exhibits the most prominent first order indices, and hence the highest sensitivities, for two factors: the liquid fuel temperature T_{liq}, and the swirl angle of the droplets Ψ_D. The temperature of the liquid fuel droplets is closely linked with the time it takes for them to evaporate, affecting the transfer of fuel from the liquid to gaseous state. This impacts the axial position at which the flame becomes stable above the atomizer. The swirl angle of the droplets determines wether the droplets are injected in a wider or narrower swirl movement around the z-axis (see Fig. 6) and hence influences the distribution of liquid and evaporated fuel in the reaction zone. This could explain the high sensitivity of the flame lift-off to this quantity. Although a similar effect should apply to the droplet's axial angle, the first order index for φ_D with respect to the lift-off height is significantly lower then for Ψ_D. However, this could be a result of the smaller uncertainty in Ψ_D then in φ_D (see Table 4). Mean gas velocity along the prefilmer U_G and especially the doplet's injection velocity U_D show a minor direct contribution to the variation in the flame lift-off height. The degree to which interaction between the input parameters contribute to this variation is indicated by the total Sobol' indices. For all parameters, $S^T, i >> S_{1,i}$ and $S^T, i - S_{1,i} \approx$ constant, indicating that there is a substantial but equal degree of interaction between all input parameters.

Regarding the flame length, first order Sobol' indices in the right hand part of Fig. 19 indicate that this quantify is mainly influenced by the two droplet inject angles φ_D and Ψ_D. Although the degree of uncertainty is distinctly different between the two inputs,
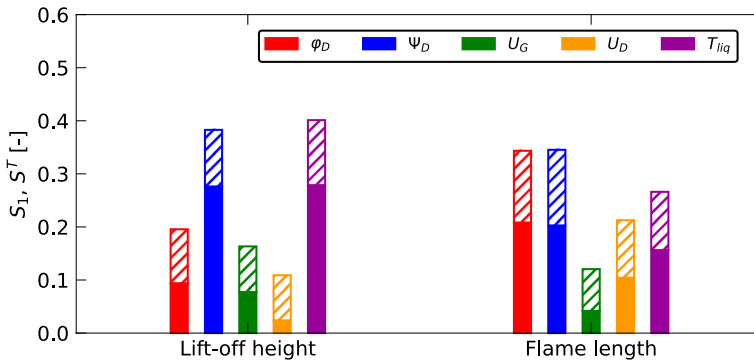
Fig. 19 First order and total Sobol' indices for flame lift-off height and flame length. Hatched bars indicate total indices

$S_{1,\varphi_D} = S_{1,\Psi_d}$ as well as $S^T_{\varphi_D} = S^T_{\Psi_d}$. Hence, the sensitivity and the degree of interaction is the same for both inputs (Fig. 19).

5 Summary and Conclusions

The present study succesfully demonstrated the application of probabilistic modeling to quantify uncertainties in the simulation of a complex, semi-technical combustor burning a multicomponent liquid fuel. The DLR *Standard Spray Burner* (SSB) constituted a simulation problem reflecting characteristics typically found in modern aeroengine combustors. In order to resolve the complex three-dimensional and unsteady flow structure, hybrid URANS/LES was utilized. To overcome the dependency from the experimental data for the spray phase—i.e. the need for calibration against existing data, an algebraic primary breakup model was incorporated. The resulting reduction in prior knowledge was compensated through probabilistic modeling and uncertainty quantification methods. The breakup model provided data for the mean diameter in the spray, but no information regarding the droplet velocities. The velocity vector of the droplets at the boundary condition was estimated from the local gas field and treated as uniformly distributed uncertainties. Further uncertainties regarding the spray boundary condition resulted in a six-dimensional parameter space of uncertain inputs. Due to their importance in the design process, temperature distribution and flame position were considered as the main quantities of interest. Output uncertainties in the simulation were then quantified through Polynomial Chaos Expansion. Moderate uncertainties were found in the results for the gas phase temperature as well as the droplet velocities. This was further confirmed by accuracy metrics comparing the probabilistic simulation results with the experimental data. A thorough analysis of the dispersed phase under uncertainties verified the assumption made in the definition of the spray boundary condition that the droplet starting velocities can be derived from the local gas velocities. Finally, a sensitivity analysis utilizing Sobol' indices revealed that the variation in the flame lift-off height is mainly induced by the uncertainties in the temperature of the liquid droplets as well as the swirl angle of the droplets, while the flame length is mostly sensitive to the uncertainties in the droplet's axial and swirl angle at the spray boundary condition.

On the basis of these results, the following conclusions are drawn:

– Propagation of uncertainties through coupling effects: The present work focused on input uncertainties in the spray boundary conditions. Hence, input uncertainties were primarily introduced to the dispersed phase of the reacting multiphase system. However, it was identified that these uncertainties affect quantities of interest in the dispersed and the continuous phase (e.g. gas phase temperature and velocity or flame position). This highlighted the propagation of input uncertainties through coupling effects throughout the entire thermo-chemical process of multiphase combustion. In view of this fact it is important to note that other input uncertainties which were not considered in the present study should be analyzed. For example, uncertainties in the chemical reaction rates would alter the temperature field and thus influence the local evaporation of droplets.
– Interpretation of uncertain simulation results: Uniformly distributed uncertainties were presumed in the SSB case which enabled the calculation of probability intervals for the uncertain simulation results. This yielded a *best estimated prediction* of the quantities of interest under the given uncertainties. It should be pointed out that this best estimate purely relied on the assumption of uniform input uncertainties. In contrast, probability bounds from Probabibilty Bounds Analysis as demonstrated in Enderle and Rauch (2020) are known to be larger (Oberkampf 2010) but always reflect the state of knowledge without further assumptions. Therefore, the impact of the application of different UQ frameworks needs to be further studied.
– Potential of UQ in the simulation of spray combustion: The present study clearly demonstrated the added value of uncertainty quantification when only limited data regarding the spray boundary conditions is available. With the additional information concerning the uncertainties in the simulation results, risks can be quantified by comparing the uncertainties with the performance targets. Thereby, decision-making in the design and development process can be supported and advanced towards risk-informed decision-making.
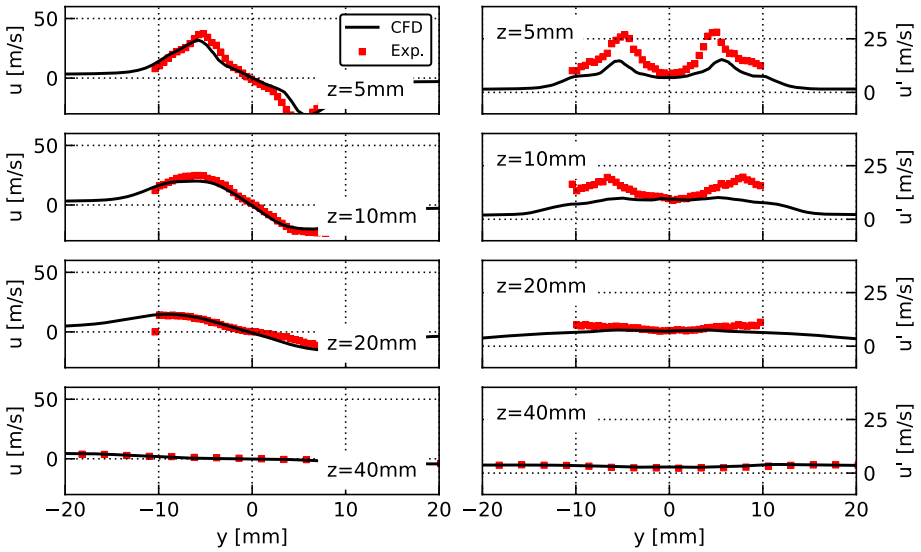
A: Additional Figures

See Figs. 20, 21, 22 and 23.
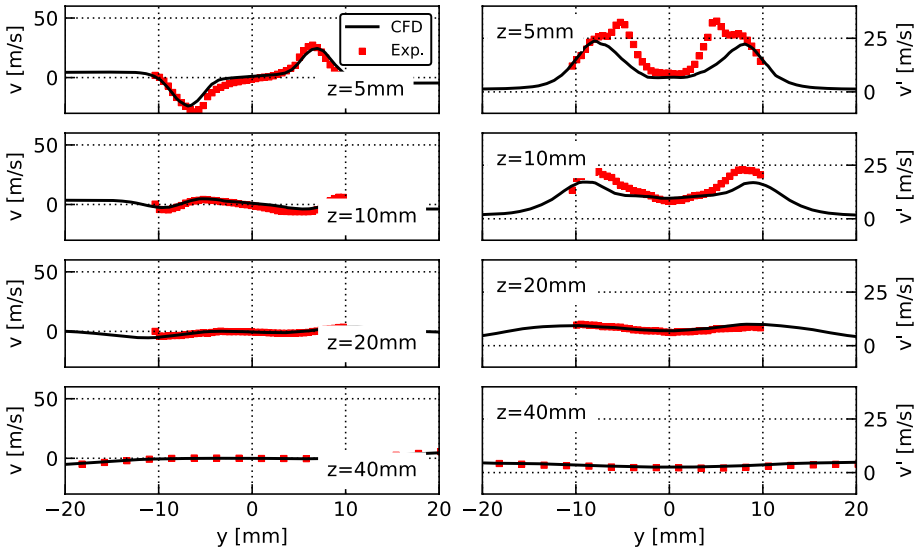
Fig. 20 Time-averaged profiles of *v* velocity component at different axial positions from cold flow measurements and simulation. Mean (left column) and RMS (right column)

Fig. 21 Time-averaged profiles of *u* velocity component at different axial positions from cold flow measurements and simulation. Mean (left column) and RMS (right column)
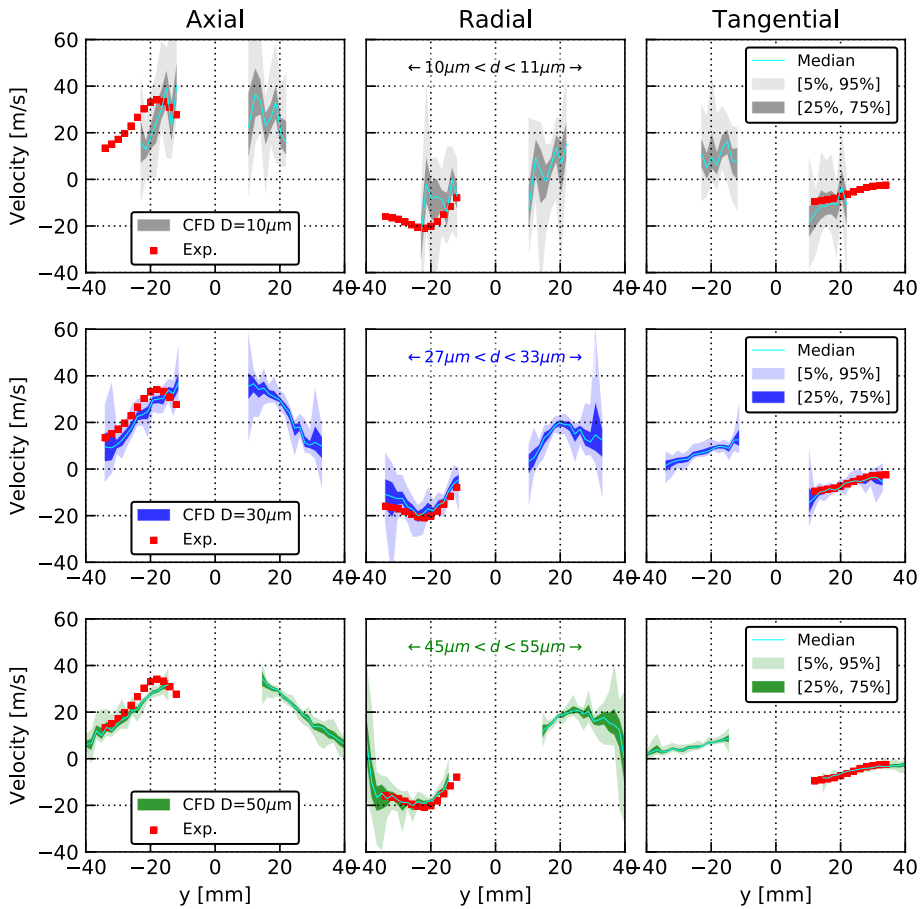
Fig. 22 Non-deterministic simulation results for time averaged profiles of droplet velocity components at $z = 25$ mm. Simulation data is split into small (■), medium (■), and large droplets (■). Experimental data (■) is averaged over all diameters

(a) SMD   (b) liquid volume flux
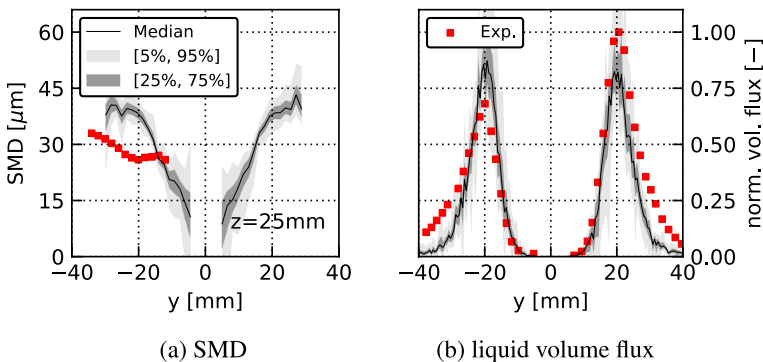
Fig. 23 Non-deterministic simulation results for time averaged profiles of Sauter Mean Diameter (SMD) and normalized liquid volume flux at $z = 25$ mm

Declarations

Conflict of interest The authors declare that they have no conflict of interest.

Ethical approval The authors complied with all ethical standards relevant to this work.

Informed consent Does not apply to this work.

References

Abramzon, B., Sirignano, W.: Droplet vaporization model for spray combustion calculations. Int. J. Heat Mass Transf. **32**(9), 1605–1618 (1989)

Bengtsson, T., Bickel, P. et al.: Curse-of-dimensionality revisited: collapse of the particle filter in very large scale systems. In; Probability and Statistics: Essays in Honor of David A. Freedman. Institute of Mathematical Statistics, pp. 316–334 (2008)

Bini, M., Jones, W.: Large-eddy simulation of particle-laden turbulent flows. J. Fluid Mech. **614**, 207–252 (2008)

Bobkov, S., Ledoux, M.: One-dimensional empirical measures, order statistics and Kantorovich transport distances (2014)

Cantu, L.M., Grohmann, J., et al.: Temperature measurements in confined swirling spray flames by vibrational coherent anti-stokes Raman spectroscopy. Exp. Therm. Fluid Sci. **95**, 52–59 (2018)

Chaussonnet, G.: Modeling of liquid film and breakup phenomena in Large-Eddy Simulations of aeroengines fueled by airblast atomizers. Ph.D. thesis. Institut National Polytechnique de Toulouse (INP Toulouse) (2014)

Chaussonnet, G., Vermorel, O., et al.: A new phenomenological model to predict drop size distribution in Large-Eddy Simulations of airblast atomizers. Int. J. Multiph. Flow **80**, 29–42 (2016)

Davis, P.J., Rabinowitz, P.: Methods of Numerical Integration. Courier Corporation, New York (2007)

de Souza, M.V.C., Colaço, M.J., et al.: Application of the generalized polynomial chaos expansion to the simulation of an internal combustion engine with uncertainties. Fuel **134**, 358–367 (2014)

Di Domenico, M., Gerlinger, P. et al.: Numerical simulations of confined, turbulent, lean, premixed flames using a detailed chemistry combustion model. In: Proceedings of ASME 2011 Turbo Expo. American Society of Mechanical Engineers, pp. 519–530 (2011)

Domenico, M.D.: Numerical simulations of soot formation in turbulent flows. Eng. Ph.D. thesis. Universität Stuttgart (2008)

Doué, N., Le Clercq, P. et al.: Validation of a multicomponent-fuel droplet evaporation model based on continuous thermodynamics. In: Proceeding of ICLASS 2006 (2006)

Dryer, F.L.: Chemical kinetic and combustion characteristics of transportation fuels. Proc. Combust. Inst. **35**(1), 117–144 (2015)

Duraisamy, K., Alonso, J.: Adjoint based techniques for uncertainty quantification in turbulent flows with combustion. In: 42nd AIAA Fluid Dynamics Conference and Exhibit, p. 2711 (2012)

Eckel, G.: Large Eddy Simulation of Turbulent Reacting Multi-Phase Flows. Ph.D. thesis. Universität Stuttgart (2018)

Eckel, G., Grohmann, J., et al.: LES of a swirl-stabilized kerosene spray flame with a multi-component vaporization model and detailed chemistry. Combust. Flame **207**, 134–152 (2019)

Enderle, B., Rauch, B., et al.: Non-intrusive uncertainty quantification in the simulation of turbulent spray combustion using Polynomial Chaos expansion: a case study. Combust. Flame **213**, 26–38 (2020)

Fishman, G.: Monte Carlo: Concepts, Algorithms, and Applications. Springer, Berlin (2013)

Forrester, A., Keane, A., et al.: Engineering Design via Surrogate Modelling: A Practical Guide. John, New York (2008)

Gepperth, S., Guildenbecher, D. et al.: Pre-filming primary atomization: Experiments and modeling. In: 23rd European Conference on Liquid Atomization and Spray Systems (ILASS-Europe 2010), pp. 6–8 (2010)

Gerlinger, P.: Numerische Verbrennungssimulation: Effiziente numerische Simulation turbulenter Verbrennung. Springer, Berlin (2005)

Ghanem, R., Ghiocel, D.: Stochastic seismic soil-structure interaction using the homogeneous chaos expansion. In: Proceedings of the 12th ASCE Engineering Mechanics Division Conference, La Jolla, California (1998)

Ghanem, R.G., Spanos, P.D.: Stochastic Finite Element Method: Response Statistics. A Spectral Approach, Stochastic Finite Elements, pp. 101–119. Springer, Berlin (1991)

Girimaji, S.: Assumed β-pdf model for turbulent mixing: validation and extension to multiple scalar mixing. Combust. Sci. Technol. **78**(4–6), 177–196 (1991)

Gneiting, T., Raftery, A.E.: Strictly proper scoring rules, prediction, and estimation. J. Am. Stat. Assoc. **102**(477), 359–378 (2007)

Goodwin, D.G., Moffat, H.K. et al.: Cantera: an object-oriented software toolkit for chemical kinetics, thermodynamics, and transport processes (2018)

Grohmann, J.: Experimentelle Untersuchungen zum Einfluss von Kohlenwasserstoffen auf das Verbrennungsverhalten drallstabilisierter Sprayflammen. Ph.D. thesis. Universität Stuttgart (2019)

Grohmann, J., Rauch, B. et al.: Investigation of differences in lean blowout of liquid single-component fuels in a gas turbine model combustor. In: 52nd AIAA/SAE/ASEE Joint Propulsion Conference, p. 4647 (2016)

Grohmann, J., Rauch, B., et al.: Influence of single-component fuels on gas-turbine model combustor lean blowout. J. Propul. Power **34**(1), 97–107 (2017)

Guo, S., Silva, C.F. et al.: Evaluating the impact of uncertainty in flame impulse response model on thermoacoustic instability prediction: a dimensionality reduction approach. In: Proceedings of the Combustion Institute (2018)

Homma, T., Saltelli, A.: Importance measures in global sensitivity analysis of nonlinear models. Reliab. Eng. Syst. Saf. **52**(1), 1–17 (1996)

Hubbard, G., Denny, V., et al.: Droplet evaporation: effects of transients and variable properties. Int. J. Heat Mass Transf. **18**(9), 1003–1008 (1975)

Ivanova, E.: Numerical simulations of turbulent mixing in complex flows. Eng. Ph.D. thesis. Universität Stuttgart (2012)

Jenny, P., Roekaerts, D., et al.: Modeling of turbulent dilute spray combustion. Prog. Energy Combust. Sci. **38**(6), 846–887 (2012)

Johnson, R., Wu, H., et al.: A general probabilistic approach for the quantitative assessment of LES combustion models. Combust. Flame **183**, 88–101 (2017)

Jones, W., Marquis, A., et al.: Large-eddy simulation of spray combustion in a gas turbine combustor. Combust. Flame **161**(1), 222–239 (2014)

Kapur, J.N., Kesavan, H.K.: Entropy optimization principles and their applications. In: Entropy and Energy Dissipation in Water Resources, pp. 3–20. Springer (1992)

Kathrotia, T.: Reaction kinetics modeling of OH*, CH*, and C2* chemiluminescence. Ph.D. thesis. Universität Heidelberg (2011)

Khalil, M., Lacaze, G., et al.: Uncertainty quantification in LES of a turbulent bluffbody stabilized flame. Proc. Combust. Inst. **35**(2), 1147–1156 (2015)

Klein, M., Sadiki, A., et al.: A digital filter based generation of inflow data for spatially developing direct numerical or large eddy simulations. J. Comput. Phys. **186**(2), 652–665 (2003)

Le Maître, O., Knio, O.M.: Stochastic spectral methods for uncertainty quantification. In: Proceedings of the 38th Conference of Dutch-Flemish NA Communities, Woudschoten (2017)

Le Maître, O., Knio, O.M.: Spectral Methods for Uncertainty Quantification: With Applications to Computational Fluid Dynamics. Springer, Berlin (2010)

Lefebvre, A.: Atomization and Sprays, vol. 1040, p. 2756. CRC Press, New York (1988)

Lefebvre, A.H.: Gas Turbine Combustion. CRC Press, New York (2010)

Loeven, G., Witteveen, J. et al.: Probabilistic collocation: an efficient non-intrusive approach for arbitrarily distributed parametric uncertainties. In: 45th AIAA Aerospace Sciences Meeting and Exhibit, p. 317 (2007)

Lourier, J.-M., Eberle, C. et al.: Influence of turbulence-chemistry interaction modeling on the structure and the stability of a swirl-stabilized flame. In: Turbo Expo: Power for Land, Sea, and Air, Vol. 56697. American Society of Mechanical Engineers (2015), V04BT04A008

Lucca-Negro, O., O'Doherty, T.: Vortex breakdown: a review. Prog. Energy Combust. Sci. **27**(4), 431–481 (2001). (**ISSN: 0360-1285**)

Masquelet, M., Yan, J. et al.: Uncertainty quantification in large eddy simulations of a rich-dome aviation gas turbine. In: Proceedings of ASME Turbo Expo 2017. American Society of Mechanical Engineers, pp GT2017–64835 (2017)

McKay, M.D., Beckman, R.J., et al.: Comparison of three methods for selecting values of input variables in the analysis of output from a computer code. Technometrics **21**(2), 239–245 (1979)

Menter, F.R.: Best practice: scale-resolving simulations in ANSYS CFD. In: ANSYS Germany GmbH 1 (2012)

Menter, F., Egorov, Y.: A scale adaptive simulation model using two-equation models. In: 43rd AIAA Aerospace Sciences Meeting and Exhibit, p. 1095 (2005)

Menter, F., Kuntz, M., et al.: A scale-adaptive simulation model for turbulent flow predictions. In: 41st Aerospace Sciences Meeting and Exhibit, p. 767 (2003a)

Menter, F.R., Kuntz, M., et al.: Ten years of industrial experience with the SST turbulence model. Turbul. Heat Mass Transf. **4**(1), 625–632 (2003)

Mercier, R., Schmitt, T., et al.: The influence of combustion SGS submodels on the resolved flame propagation. Application to the LES of the Cambridge stratified flames. Proc. Combust. Inst. **35**(2), 1259–1267 (2015)

Methling, T.: Entwicklung des linearen Transformationsmodells für die Analyse und Optimierung chemisch-kinetischer Prozesse. Ph.D. thesis. Universität Stuttgart (2017)

Mueller, M.E., Iaccarino, G., et al.: Chemical kinetic uncertainty quantification for large eddy simulation of turbulent nonpremixed combustion. Proc. Combust. Inst. **34**(1), 1299–1306 (2013)

Müller, A., Meier, R. et al.: The influence of unsteady flow conditions on liquid sheet atomisation. In: Atomization and Spray Processes, pp. 134–138 (2004)

Najm, H.N.: Uncertainty quantification and polynomial chaos techniques in computational fluid dynamics. Annu. Rev. Fluid Mech. **41**, 35–52 (2009)

Nau, P., Yin, Z. et al.: Wall temperature measurements in gas turbine combustors with thermographic phosphors. J. Eng. Gas Turbin. Power **141**(4) (2019)

Oberkampf, W.L.C.: Verification and Validation in Scientific Computing. Cambridge University Press, Cambridge (2010)

Pei, Y., Davis, M.J., et al.: Engine combustion network (ECN): global sensitivity analysis of spray a for different combustion vessels. Combust. Flame **162**(6), 2337–2347 (2015)

Poinsot, T., Veynante, D.: Theoretical and Numerical Combustion. RT Edwards Inc, London (2005)

Pope, S.B.: Ten questions concerning the large-eddy simulation of turbulent flows. New J. Phys. **6**(1), 35 (2004)

Reagan, M.T., Najm, H.N., et al.: Uncertainty quantification in reacting-flow simulations through non-intrusive spectral projection. Combust. Flame **132**(3), 545–555 (2003)

Reagan, M., Najm, H., et al.: Spectral stochastic uncertainty quantification in chemical systems. Combust. Theor. Model. **8**(3), 607–632 (2004)

Red-Horse, J., Benjamin, A.S.: A probabilistic approach to uncertainty quantification with limited information. Reliab. Eng. Syst. Saf. **85**(1–3), 183–190 (2004)

Roy, C.J., Oberkampf, W.L.: A comprehensive framework for verification, validation, and uncertainty quantification in scientific computing. Comput. Methods Appl. Mech. Eng. **200**(25), 2131–2144 (2011)

Ruoff, S.J., Rauch, B. et al.: Assessment of the comparability of droplet evaporation fuel sensitivities between a unit test case and an aviation gas turbine combustor. In: AIAA Scitech 2019 Forum, p. 0727 (2019)

Ruoff, S., Stöhr, M., et al.: Numerical simulation and uncertainty quantification of a generic droplet evaporation validation test case. Atomiz. Sprays **30**(12), 861–879 (2020)

Setzwein, F., Ess, P., et al.: Large-Eddy simulation of spray flames in the DLR generic single sector combustor. In: AIAA Propulsion and Energy 2019 Forum, p. 3865 (2019)

Sheen, D.A., Wang, H.: The method of uncertainty quantification and minimization using polynomial chaos expansions. Combust. Flame **158**(12), 2358–2374 (2011)

Slavinskaya, N.: Skeletal mechanism for kerosene combustion with PAH production. In: Proceedings of 46th AIAA Aerospace Sciences Meeting and Exhibit, Reno (USA), Paper. 0992 (2008)

Sobol, I.M.: Sensitivity estimates for nonlinear mathematical models. Math. Model. Comput. Exp. **1**(4), 407–414 (1993)

Sobol, I.M., Asotsky, D., et al.: Construction and comparison of high-dimensional Sobol' generators. Wilmott **2011**(56), 64–79 (2011)

Sudret, B.: Uncertainty propagation and sensitivity analysis in mechanical models-contributions to structural reliability and stochastic spectral methods. In: Habilitation a diriger des recherches, p. 18. Université Blaise Pascal, Clermont-Ferrand (2007)

Tanner, F.X.: A cascade atomization and drop breakup model for the simulation of high-pressure liquid jets. Technical report, SAE Technical Paper (2003)

Tropea, C.: Optical particle characterization in flows. Annu. Rev. Fluid Mech. **43**, 399–426 (2011)

Van Dam, N., Rutland, C.: Uncertainty quantification of large-eddy spray simulations. J. Verific. Valid. Uncertain. Quantif. **1**(2), 021006 (2016)

Xiu, D., Karniadakis, G.E.: The Wiener–Askey polynomial chaos for stochastic differential equations. SIAM J. Sci. Comput. **24**(2), 619–644 (2002)

Yondo, R., Andrés, E., et al.: A review on design of experiments and surrogate models in aircraft real-time and many-query aerodynamic analyses. Prog. Aerosp. Sci. **96**, 23–61 (2018)